

SHAP zero Explains Genomic Models with Near-zero Marginal Cost for Future Queried Sequences

Darin Tsui¹, Aryan Musharaf², Yigit Efe Erginbas³, Justin Singh Kang³, and Amirali Aghazadeh^{1,*}

¹School of Electrical and Computer Engineering, Georgia Institute of Technology

²School of Computer Science, Georgia Institute of Technology

³Department of Electrical Engineering and Computer Sciences,
University of California Berkeley

*Correspondence to: Amirali Aghazadeh: amiralia@gatech.edu

Abstract

With the rapid growth of large-scale machine learning models in genomics, Shapley values have emerged as a popular method for model explanations due to their theoretical guarantees. While Shapley values explain model predictions locally for an individual input query sequence, extracting biological knowledge requires global explanation across thousands of input sequences. This demands exponential model evaluations per sequence, resulting in significant computational cost and carbon footprint. Herein, we develop SHAP zero, a method that estimates Shapley values and interactions with a near-zero marginal cost for future queried sequences after paying a one-time fee for model sketching. SHAP zero achieves this by establishing a surprisingly underexplored connection between the Shapley values and interactions and the Fourier transform of the model. Explaining two genomic models, one trained to predict guide RNA binding and the other to predict DNA repair outcome, we demonstrate that SHAP zero achieves orders of magnitude reduction in amortized computational cost compared to state-of-the-art algorithms, revealing almost all predictive motifs—a finding previously inaccessible due to the combinatorial space of possible interactions.

1 Introduction

Shapley values have emerged as a theoretically robust method for explaining the local additive features of an input query to a black-box model [1–3]. Extracting biological knowledge from the emerging models in genomics, however, demands a global understanding, which requires explaining the *interactions among features* and doing so for *hundreds to thousands of input query sequences*. Unfortunately, finding Shapley values and interactions has a high computational cost, with an exact calculation requiring an exponential number of model evaluations in the input dimension [4]. With the increasing growth of large-scale machine learning models in genomics [5], often with only proprietary access, there is an urgent need for methods to explain these black-box models faster, more efficiently, and with a lower carbon footprint.

Consider the problem of explaining a black-box model that takes in a length- n DNA sequence in $\{A, T, C, G\}^n$ and outputs a real number. We denote this model as the function $f(\mathbf{x})$ with the input vector $\mathbf{x} \in \mathbb{Z}_{q=4}^n = \{0, 1, 2, 3\}^n$, encoding for the DNA sequence with $q = 4$ alphabets. One popular method of explaining the prediction of $f(\mathbf{x})$ to the input query sequence \mathbf{x} is using SHapley Additive exPlanations (SHAP) [6]. SHAP explains the output of $f(\mathbf{x})$ by assigning a so-called SHAP value $I^{SV}(i)$ to the i^{th} nucleotide in \mathbf{x} , where i belongs to the feature set $D = \{1, 2, \dots, n\}$ (Fig. 1a):

$$I^{SV}(i) = \sum_{T \subseteq D \setminus \{i\}} \frac{|T|!(|D| - |T| - 1)!}{|D|!} [v_{T \cup \{i\}}(\mathbf{x}) - v_T(\mathbf{x})]. \quad (1)$$

$I^{SV}(i)$ computes the marginal contribution of the i^{th} nucleotide to the value function $v_T(\mathbf{x})$ for all the subsets T of features in $D \setminus \{i\}$. There are several ways to define the value function [7]. For genomic problems where we are restricted to four possible nucleotides, we consider the value function as $v_T(\mathbf{x}) = \frac{1}{q^{|\bar{T}|}} \sum_{\mathbf{m}: \mathbf{m}_{\bar{T}} \in \mathbb{Z}_q^{|\bar{T}|}, \mathbf{m}_T = \mathbf{x}_T} f(\mathbf{m})$, which marginalizes the effect of absent nucleotides in $\bar{T} = D \setminus T$ by taking an average contribution over $q^{|\bar{T}|}$ possible inputs (see Fig. 1a and Equation (4) in Methods). SHAP requires computing $v_T(\mathbf{x})$ for every subset of features in $T \subseteq D$, which means evaluating $f(\mathbf{x})$ using a number of samples that grows exponentially with n . The algorithms to approximately compute SHAP values are either stochastic estimators [6, 8–12] or model-based approximators [6, 13–18]. Stochastic estimators, such as KernelSHAP [6], randomly subsample the feature subsets ($T, v_T(\mathbf{x})$) and approximately solve a weighted-least squares problem to estimate $I^{SV}(i)$. These algorithms require many model evaluations and impose an undesirable trade-off between sample complexity and accuracy [19]. Model-based approximators, such as DeepSHAP [6], use the model architecture to estimate Shapley values. These methods are often faster but still require many model evaluations and only work for white-box models. Algorithms to compute Shapley interactions in black-box models [20–23], such as SHAP-IQ [20], subsample feature interactions for efficiency but similar to stochastic estimators they need many model evaluations.

To empirically demonstrate how current SHAP algorithms scale, consider TIGER [24], a recent model that predicts the efficiency of CRISPR-Cas13d guide RNA from their sequence and context. SHAP values and interactions explain which regions in the guide RNA is the most determinant of

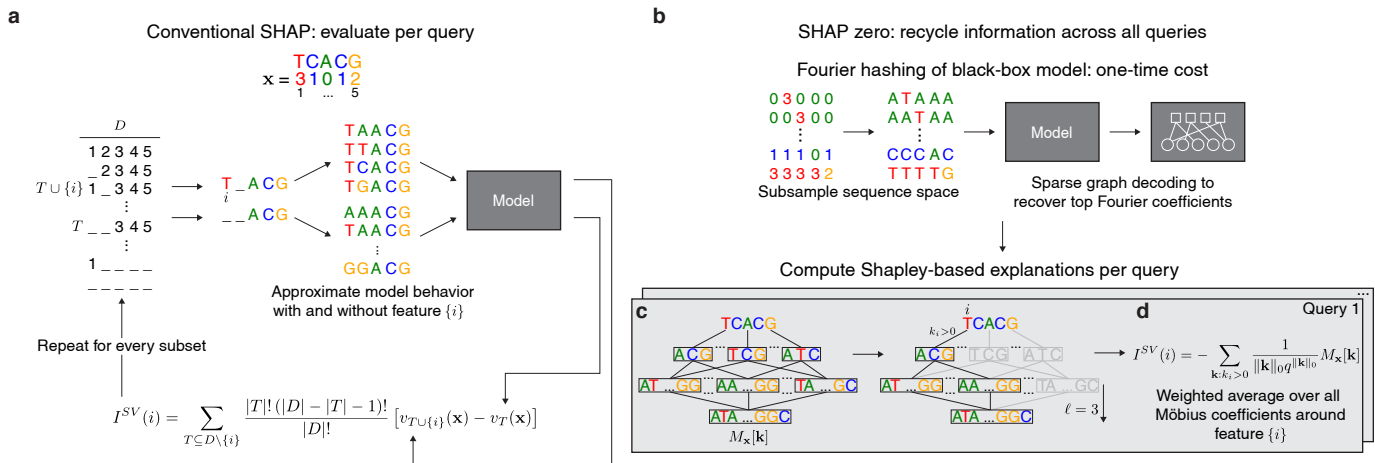


Figure 1: **Schematic of the flowchart for the exact computation of SHAP Additive explanations (SHAP) and our approximation method SHAP zero.** **a**, Computing SHAP values exactly requires exponential model evaluations with sequence length n , per query sequence. This illustration shows computing one such term in $I^{SV}(i = 1)$, which measures the marginal contribution of the nucleotide T at site $i = 1$ to the set $T = \{3, 4, 5\}$ by evaluating the model for all four possible nucleotides at $D \setminus (T \cup \{i\}) = \{2\}$ to compute $v_{T \cup \{i\}}(\mathbf{x})$ and all $4^2 = 16$ possible nucleotide combinations at $D \setminus T = \{1, 2\}$ to compute $v_T(\mathbf{x})$. **b**, In contrast, SHAP zero cleverly samples the sequence space and resolves a sparse bipartite graph to approximate the original model with its top- s Fourier coefficients. **c**, For each query sequence \mathbf{x} , SHAP zero maps the top- s Fourier coefficients into the Möbius transform $M_{\mathbf{x}}[\mathbf{k}]$, where \mathbf{k} is the feature interaction vector. The illustration shows one such sequence’s Möbius transform, composed of all the permutations of $\ell = 3$ nucleotides from the original sequence. **d**, SHAP zero computes $I^{SV}(i = 1)$ using a weighted sum of the Möbius coefficients with $k_1 > 0$ (Equation (2)). SHAP zero amortizes the cost of finding the Fourier transform over the future explanations.

efficiency. We estimated KernelSHAP [6] values of all the nucleotides in 1038 sequences in the training set. This took about one day on our single NVIDIA RTX A6000 machine. Worse yet, computing Faithful Shapley Interaction index (Faith-Shap) [21] to find up to third-order feature interactions using SHAP-IQ estimated to take more than 81 days—revealing a severe scalability issue in current explainability methods.

We posit that the model evaluations needed to estimate the SHAP values of an input query sequence have information that can be used to estimate the SHAP values for a new query sequence. Therefore, instead of independently evaluating the model for each query sequence, one can “recycle” the model evaluations to slash the sample and computational cost of explaining the model. Taking this idea to the extreme, we propose to do initial query-agnostic model evaluations to *sketch* the model and then use the sketch for model explanation. How can a model be sketched to be efficiently mapped to SHAP values and Shapley interactions? We uncover a surprisingly underexplored connection between SHAP values and interactions and the model’s Fourier transform, enabling us to sketch the model and use the

sketch for fast Shapley explanations. The Fourier transform provides a *global* sketching of the model $f(\mathbf{x})$ irrespective of the query sequence or even the training distribution. Moreover, since Fourier is an orthonormal basis, it enables a fast and sample-efficient method for sketching black-box models in genomics that are compressible or near-sparse in the Fourier domain [25–28].

Herein, we develop SHAP zero, a method that estimates SHAP values and Shapley interactions with a *near-zero additional cost per new query sequence* after paying an initial up-front cost for model sketching (Fig. 1b). In developing SHAP zero, we make three distinct and interconnected contributions: First, we build on the existing algorithms in sparse Fourier transforms [28, 29] and develop a method to sketch a black-box model $f(\mathbf{x})$ with sequence input (defined over q alphabets) and real-valued output, in terms of its top- s Fourier coefficients with a sample complexity of $\mathcal{O}(sn^2)$ and a computational complexity of $\mathcal{O}(sn^3)$. Second, we establish a mathematical formalism to map from (i) the Fourier transform to a transform from algebraic geometry called the Möbius transform and (ii) from the Möbius transform to Shapley-based explanations. The Möbius transform [30, 31] enables us to map the top- s Fourier coefficients of the model $f(\mathbf{x})$ to Shapley-based explanations in $\mathcal{O}(s^2(2q)^\ell)$ time per query sequence, where ℓ is the maximum order of Fourier interactions recovered by SHAP zero, in practice, bounded by $\ell \leq 5$ [32]. Third, we conduct large-scale experiments to explain two genomic models, TIGER [24] and inDelphi [33], with SHAP zero. We demonstrate that SHAP zero estimates feature interactions with an amortized computational cost up to 1000-fold faster than current methods. SHAP zero reveals the GC content of the seed region in TIGER and microhomologous motifs in inDelphi as predictive high-order features, a task previously inaccessible due to the combinatorial space of possible feature interactions.

2 Results

The SHAP zero algorithm. SHAP zero estimates SHAP values and interactions in three steps. First, it pays a one-time cost to estimate the top- s Fourier coefficients of the model $f(\mathbf{x})$. It cleverly subsamples the model in the sequence space to linearly hash the Fourier coefficients into buckets, resulting in a sparse bipartite graph (Fig. 1b). SHAP zero then recovers the top- s Fourier coefficients by resolving the graph using a peeling procedure [28, 34] with a sample complexity of $\mathcal{O}(sn^2)$ and a computational complexity of $\mathcal{O}(sn^3)$. Second, SHAP zero maps the top- s Fourier coefficients to the Möbius transform $M_{\mathbf{x}}[\mathbf{k}]$ around each input query sequence \mathbf{x} , where $\mathbf{k} \in \mathbb{Z}_q^n$ is the feature interaction vector. Computing this mapping has a complexity of $\mathcal{O}(s^2(2q)^\ell)$ (see Fig. 1c and Equation (13) in Methods). Third, SHAP zero maps the Möbius transform to $I^{SV}(i)$ using,

$$I^{SV}(i) = - \sum_{\mathbf{k}:k_i>0} \frac{1}{\|\mathbf{k}\|_0 q^{\|\mathbf{k}\|_0}} M_{\mathbf{x}}[\mathbf{k}], \quad (2)$$

with a computational complexity of $\mathcal{O}(q^\ell)$. Here, $q = 4$, the $>$ operation is defined over the standard real field in \mathbb{Z}_q^n , and the L_0 norm $\|\mathbf{k}\|_0$ counts the number of nonzero elements in \mathbf{k} (Fig. 1d). $I^{SV}(i)$

can be interpreted as the contribution of the i^{th} nucleotide to the prediction of $f(\mathbf{x})$; when $I^{SV}(i) > 0$, substituting the i^{th} nucleotide to a different nucleotide will, on average, decrease the value of $f(\mathbf{x})$, and vice versa. Therefore, $I^{SV}(i)$ sums over Möbius transform coefficients, which capture the marginal effects of all subsets of features on $f(\mathbf{x})$, with a negative sign. SHAP zero maps the Möbius transform to the ℓ^{th} order Faith-Shap interaction index $I^{FSI}(T)$ using $I^{FSI}(T) = (-1)^{|T|} \sum_{\mathbf{k}: \mathbf{k}_T > \mathbf{0}_{|T|}} \frac{1}{q^{|\mathbf{k}|_0}} M_{\mathbf{x}}[\mathbf{k}]$, with a computational complexity of $\mathcal{O}(q^\ell)$. Faith-Shap can be seen as a generalization of the SHAP value for feature interactions [21]; when $\ell = 1$, computing Faith-Shap interactions becomes identical to computing SHAP values using Equation (2). Notably, after paying a one-time cost to find the top- s Fourier coefficients, which scale with $\text{poly}(n)$, finding SHAP values and interactions from the top- s Fourier coefficients do not have computation dependency on n and only grow with s . Moreover, the exponential dependence of the bound $\mathcal{O}(s^2(2q)^\ell)$ with the maximum order of interactions ℓ does not impact SHAP zero in practice since ℓ is typically a small constant for all models in genomics. This enables SHAP zero to explain a new query sequence with near-zero cost (essentially free) in addition to the one-time cost paid for model sketching.

Explaining Guide RNA Binding. TIGER [24] is a convolutional neural network trained to predict the binding efficiency of CRISPR-Cas13d guide RNA (gRNA) to a target DNA sequences (Fig. 2a). We considered length- $n = 26$ input sequences to the model that perfectly match the target and guide RNA sequences that reverse complement the target. Positions 6-12 of the target sequence correspond to the nucleotides that bind with the seed region in the gRNA: a short segment that facilitates the initial pairing with the target [35] and is especially sensitive to mutations [36].

We first evaluated the accuracy of the recovered Fourier coefficients used to estimate SHAP zero by predicting the experimental guide scores of 1038 held-out target sequences (Fig. 2b). SHAP zero’s recovered Fourier coefficients predict experimental guide scores with a Pearson correlation of $\rho = 0.58$, outperforming the linear ($\rho = 0.44$) and pairwise ($\rho = 0.48$) model with L2 regularization, suggesting that it successfully captures high-order feature interactions. SHAP zero and KernelSHAP estimates are in high agreements ($\rho = 0.83$), with 47% and 56% of their top positive estimates attributed to C and G nucleotides in the seed region, respectively, highlighting the GC content as a predictive feature (see Fig. 2c, Table S1, and Table S2). However, it took us an amortized time of only 6.5 seconds to compute SHAP zero values compared to 109 seconds to find KernelSHAP values (Fig. 2d), a 17-fold speedup.

We then explained the high-order feature interactions with SHAP zero and compared it with SHAP-IQ. The overlapping interactions in SHAP zero and SHAP-IQ, constituting 95% and 5% of the total interactions, respectively, correlate with $\rho = 0.79$. We expected most interactions to be located within the seed region [24, 37]; however, we observed that only 34% of SHAP-IQ’s interactions are within the seed region, compared to 52% of SHAP zero’s interactions (Fig. 2e). Besides, estimating the Faith-Shap interactions took an amortized time of 6.5 seconds for SHAP zero compared to 2 hours for SHAP-IQ (Fig. 2f), suggesting that SHAP zero is more than 1000-fold faster and enables a biologically feasible explanation of feature interactions.

Explaining DNA Repair Outcome. inDelphi [33] is a machine learning model trained to predict DNA repair outcomes after CRISPR-Cas9-induced double-stranded breaks, including the probability

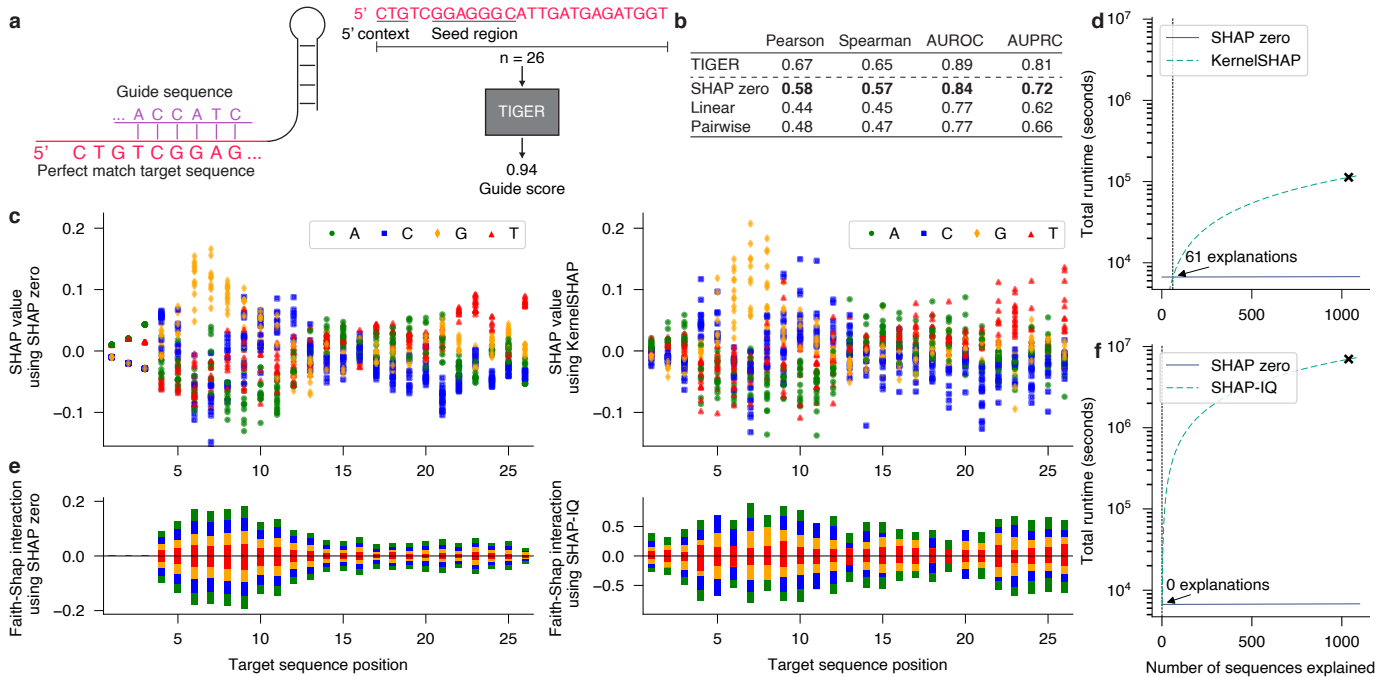


Figure 2: Explaining SHAP values and interactions in TIGER. **a**, TIGER [24] predicts the binding effects of CRISPR-Cas13d guide RNA (gRNA) sequences to target sequences. To obtain guide scores, we input length- $n = 26$ perfect match target sequences, where positions 1-3 correspond to the additional 5' context given to the target sequence and positions 6-12 correspond to the seed region [24]. **b**, The estimated top Fourier coefficients by SHAP zero outperform linear and pairwise models in predicting the guide scores in a held-out set. **c**, SHAP value estimates reveal high agreements (Pearson correlation of 0.83) between SHAP zero and KernelSHAP over 1038 query sequences (a random subset of 50 estimates shown for clarity). **d**, Total runtime of SHAP zero against KernelSHAP is marked by \times in plots that depict the computational cost versus the number of explained sequences in both algorithms. SHAP zero outperforms KernelSHAP in amortized computational cost past 61 explanations. **e**, A histogram of Faith-Shap interactions over 1038 sequences with SHAP zero and eight sequences with SHAP-IQ (see interaction details in Supplementary Table S3 and Supplementary Fig. S1). **f**, Total runtime of SHAP zero versus SHAP-IQ in TIGER demonstrate that SHAP zero is more than 1000-fold faster. Source data are provided as Source Data file.

of Cas9 inducing a one- or two-base pair insertion or deletion (frameshift frequency) (Fig. 3a). We considered length- $n = 40$ input DNA target sequences, where the cut site occurs between positions 20 and 21, a region that is considered to have the most predictive power [25, 33, 38].

We used the recovered Fourier coefficients from SHAP zero to predict the experimental frameshift frequencies of 84 held-out target sequences (Fig. 3b). SHAP zero predicted experimental frameshift frequencies with $\rho = 0.74$, outperforming the linear ($\rho = 0.37$) and pairwise ($\rho = 0.47$) model with L2 regularization, suggesting it captures high-order feature interactions. SHAP zero and KernelSHAP estimates are in high agreement again ($\rho = 0.84$) with 82% and 73% of the top SHAP zero and

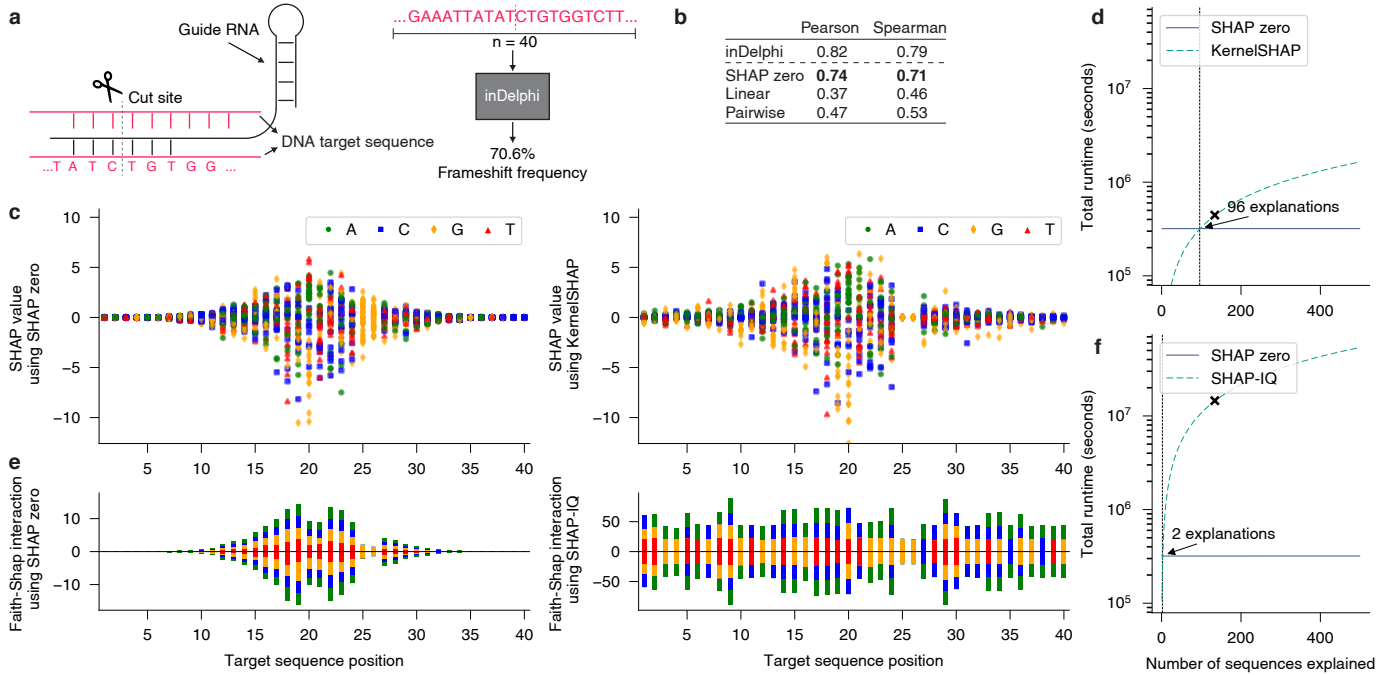


Figure 3: **Explaining SHAP values and interactions in inDelphi.** **a**, inDelphi [33] predicts DNA repair outcomes after a double-stranded break. To obtain the predicted frameshift frequency, we input length- $n = 40$ DNA target sequences, where the cut breaks the double strand between the 20 and 21 nucleotides. **b**, The recovered Fourier coefficients from SHAP zero outperform linear and pairwise models in predicting frameshift frequencies in a held-out set. AUROC and AUPRC are not reported due to the regression nature of the model (see experimental setup in Methods). **c**, SHAP value estimates exhibit a Pearson correlation of 0.84 SHAP zero and KernelSHAP over 134 query sequences and reveal the importance of nucleotides around the cut site. **d**, Total runtime of SHAP zero versus KernelSHAP. **e**, Histogram of Faith-Shap interactions run over 134 sequences with SHAP zero and four sequences with SHAP-IQ (see interaction details in Supplementary Table S6 and Supplementary Fig. S2). High-order feature interactions identified by SHAP zero reveal the importance of microhomology patterns around the cut site (see Supplementary Table S6). **f**, Total runtime of SHAP zero versus SHAP-IQ in inDelphi. Source data are provided as Source Data file.

KernelSHAP values located within three nucleotides away from the cut site, respectively (see Fig. 3c, Table S4, and Table S5 in Supplementary Materials). This time, it took SHAP zero an amortized time of 40 minutes to estimate the SHAP values compared to KernelSHAP’s 55 minutes (Fig. 3d). The difference in amortized time is smaller here than in TIGER due to the smaller set of query sequences.

We then used SHAP zero and SHAP-IQ to extract high-order feature interactions. The overlapping interactions (constituting 85% and 3% of the total interactions in SHAP-IQ and SHAP zero, respectively) correlate with $\rho = 0.74$. However, just 17% of SHAP-IQ’s interactions are within three nucleotides of the cut site compared to 55% of SHAP zero’s interactions (Fig. 3e). Similar to TIGER, we noticed a significant speedup in amortized time when using SHAP zero compared to SHAP-IQ: SHAP zero took

40 minutes compared to 37 hours from SHAP-IQ (Fig. 3f).

We performed a detailed analysis of the top SHAP zero feature interactions of inDelphi (see Table S6 in Supplementary Materials). Our analysis reveals repeating motifs around the cut site as key high-order features predictive of DNA repair [25, 33]. These high-order features can be attributed to microhomology patterns that mediate long deletions around the cut site [39]. Notably, a top feature identified by SHAP zero enriching the frameshift frequency is the repetition of the GC motif at sites 17-18 and 21-22. This feature captures the microhomology-mediated deletion of four nucleotides at 17-20, which results in a one-base pair frameshift. Another top feature identified by SHAP zero depleting the frameshift frequency is the repetition of the TC motif at sites 18-19 and 21-22. This feature captures the microhomology-mediated deletion of three nucleotides at 18-20, which results in no frameshift. These examples highlight the unique capability of SHAP zero in extracting biologically meaningfully high-order interactions, which was previously inaccessible due to the space of feature interactions.

3 Discussion

Contrasting different amortization strategies. From the amortization perspective, SHAP zero is connected with a SHAP estimation algorithm called FastSHAP [40]. FastSHAP trains a *surrogate* model (e.g., a neural network) for amortization, which takes in a vector of masked features and predicts the model output, enabling marginalization over the masked entries without a combinatorial model evaluation. Despite theoretical results which show that the global minimizer of the surrogate model will perform optimal marginalization [41], our results demonstrate that FastSHAP poorly correlate with KernelSHAP on TIGER and inDelphi models, with $\rho = -0.39$ and $\rho = 0.08$, respectively (see Fig. S3 and S4 in Supplementary Materials). We attribute this to the nature of inference problems in genomics. The surrogate model does not achieve the global minimizer because the outputs of TIGER and inDelphi are highly sensitive to the masked nucleotides in the seed region and around the cut site, respectively. In this setting, the surrogate model produces reliable marginalization only if its training data contains the model evaluations for (almost) all unmasked sequences, which is unfeasible. This is contrary to data modalities such as images, where the model output is rarely a function of a few masked pixels. SHAP zero, on the other hand, solely relies on the assumption that the mode is compressible, leading to an accurate and less biased amortization strategy with comparable speedup.

Explainability trade-offs in white-box methods. The white-box explainability methods, such as DeepSHAP [6] and DeepLIFT [13], leverage the model architecture to estimate SHAP values extremely efficiently; however, they naturally fall short in (i) estimating high-order feature interactions, and (ii) black-box settings with only query access, which is the focus of this work. Regardless, SHAP zero due to its amortized nature, outperforms these methods in computational cost *asymptotically*. Extrapolating the amortized runtimes, our results in TIGER demonstrate that SHAP zero is more efficient when the queries exceed 25,000 sequences (see Fig. S3 in Supplementary Materials).

Marginalization strategies in SHAP and connections with SHAP zero. SHAP zero’s strategy for marginalizing the effects of absent features is closest to the uniform approach in [7]. Estimating the top- s Fourier coefficients by subsampling the sequence space is made under the key assumption that all nucleotides are equally probable. This differs from other Shapley-based algorithms, which use the training distribution to marginalize against absent features [6, 7, 20, 21, 23]. An interesting extension would be to marginalize absent features using the training data distribution, which would necessitate the development of sparse Fourier algorithms capable of subsampling the sequence space while accounting for this distribution.

Connections with TreeSHAP. A notable feature of SHAP zero is the ability to approximate black-box models in their Möbius transform, which exhibits a tree-like structure. From this perspective, SHAP zero complements TreeSHAP [18], which finds SHAP values from tree-based models. Another promising future direction would be to combine TreeSHAP with SHAP zero’s Fourier-to-Möbius mapping to enhance Shapley-based computational efficiency further.

Overall, SHAP zero expands our toolkit in the explainability of machine learning models in genomics and, more broadly, in problems with a combinatorial nature. It enables us to extract and explain feature interactions that were never accessible before due to the combinatorial explosion of high-order interactions. Our work will further encourage interdisciplinary algorithms and theoretical frameworks at the intersection of signal processing, coding theory, and algebraic geometry for the benefit of explainability in machine learning.

4 Code availability

Software for SHAP zero, as well as codes to reproduce the results in this work, is available at <https://github.com/amirgroup-codes/shapzero>.

5 Data availability

Target sequence data used in Fig. 2 are available in the GitHub repository associated with [24]. DNA repair data used in Fig. 3 are available in the GitHub repository associated with [33]. All SHAP values and Faith-Shap interactions from TIGER and inDelphi used to create Fig. 2, Fig. 3, and the Supplementary Material are available in the figshare data repository under accession code 27245061. All other data generated or analyzed in this study are included in this article and its accompanying Supplemental Material.

6 Competing interests

Authors do not have any competing interests in conducting this project.

7 Author contributions

D.T. and A.A. conceived the project and designed experiments. D.T. and A.M. conducted the experiments. D.T. and A.A. analyzed the data and created the figures. D.T., Y.E.E., J.S.K., and A.A. performed the theoretical analysis of the Möbius transform and conversion from the Fourier transform. D.T. and A.A. performed the remaining theoretical analysis. D.T., A.M., Y.E.E., J.S.K., and A.A. wrote the manuscript. A.A. supervised the project.

8 Acknowledgment

This research was supported by the National Science Foundation (NSF) Graduate Research Fellowship Program (GRFP), the Parker H. Petit Institute for Bioengineering and Biosciences (IBB) interdisciplinary seed grant, the Institute of Matter and Systems (IMS) Exponential Electronics seed grant, and Georgia Institute of Technology start-up funds.

9 Methods

Experimental setup: TIGER. We considered the sequence-only implementation of TIGER by inputting length- $n = 26$ perfect match target sequences, where the model assumes that the gRNA is a perfect sequence complement of the target sequence. To recover Fourier coefficients, we applied the sparse Fourier algorithm q -SFT [28] through their GitHub repository (<https://github.com/basicslab/qsft>), setting $q = 4$ and $n = 26$. We employed the recommended q -SFT parameters, which includes setting *query_method* to “complex”, *num_subsample* and *num_repeat* to 3, *delays_method_source* to “identity”, and *delays_method_channel* to “nso”. We optimized the hyperparameters b and *noise_sd* to determine how many model evaluations to make. b controls the number of evaluations q -SFT takes, while *noise_sd* sets the peeling threshold to recover Fourier coefficients. We first increased b as much as computationally feasible on our servers. To find the optimal value of *noise_sd*, we performed a coarse search from 0 to 20 at 20 evenly spaced points and used the recovered Fourier coefficients at each level of *noise_sd* to predict the values of a test set of 10,000 samples (done by setting the test argument *n_samples* to 10,000). After finding the general range where R^2 was the largest, we refined our search within that general range at a step size of 0.025. We used $b = 7$ and *noise_sd* = 0.725, which corresponded to an R^2 of 0.55. While increasing the value of b will increase the accuracy of the recovered Fourier coefficients, we find that $b = 7$ gives us reliable SHAP estimates, as evident by the Pearson correlation with KernelSHAP.

We used the held-out perfect match target sequences provided by TIGER [24] to predict the experimental scores, which are available as a CSV file on our GitHub. We evaluated the performance of the recovered Fourier coefficients using Pearson correlation, Spearman correlation, area under the receiver operating characteristic curve (AUROC), and area under the precision-recall curve (AUPRC). AUROC and AUPRC were used because TIGER allows thresholding predictions to formulate a binary classification problem. We created our linear and pairwise interaction model baselines using sklearn in Python. Our baseline models were trained on one-hot encoded sequences using the training data from TIGER to predict the experimental guide score, employing Ridge regression with $\lambda = 0.5$. To construct the pairwise interaction model, we used sklearn’s PolynomialFeatures implementation, setting *degree* to 2 and *interaction_only* to True.

SHAP zero was run on all held-out sequences to compute SHAP values and Faith-Shap interactions. To create the KernelSHAP baseline, we used the Python package SHAP’s KernelSHAP implementation. The background dataset consists of 30 samples randomly drawn from the training set, and we compute SHAP values across all the held-out sequences. We determined the size of the background dataset by computing the KernelSHAP values on 10% of the held-out data and increasing the number of background samples in increments of 15 until the KernelSHAP values visually converged. To compute Faith-Shap interactions, we used SHAP-IQ’s implementation, available on their GitHub repository (<https://github.com/mmschlk/shapiq>). Since SHAP-IQ was computationally too expensive to run over all sequences, we randomly selected eight sequences to analyze. We used the same background dataset of 30 samples and hyperparameter tuned the parameters *max_order* (which determines the maximum order of Faith-Shap interactions to compute) and *budget* (which determines the number of model evalu-

ations to make). We increased max_order in increments of 1 and $budget$ in increments of 10,000 until the Faith-Shap interactions visually converged, or we ran into computational feasibility issues. We used $max_order = 3$ and $budget = 50,000$ in our experiments. To run FastSHAP, we used the FastSHAP implementation available on their GitHub repository (<https://github.com/iancovert/fastshap>). We removed all instances of calling the *softmax* function. We replaced the KL divergence loss used to train the surrogate neural network for mean squared error loss since the FastSHAP implementation on their GitHub is designed for classification and not regression. Following the FastSHAP implementation left on their GitHub for the census dataset, the surrogate model is implemented using a neural network consisting of three fully connected layers, where each layer is 128 units wide, with ReLU activation. We did not train the surrogate model according to their CIFAR implementation because their CIFAR-10 surrogate model uses a pre-trained ResNet-50 model designed for image-specific tasks. The surrogate model was trained on the entire training set. All other FastSHAP parameters were left as default according to their GitHub implementation on the CIFAR-10 dataset. To run DeepSHAP, we use an implementation of DeepSHAP left in the TIGER repository (<https://github.com/daklab/tiger>). DeepSHAP was implemented using the Python package SHAP. The background dataset consists of 5000 samples randomly drawn from the training set, which is the number of background samples TIGER utilizes in their own DeepSHAP implementation. All other parameters were left as default.

To determine the top SHAP values in the Supplementary Material (see Table S1 and Table S2), we separated the SHAP values into positive and negative values. For the positive and negative grouping, we calculated the average contribution of each nucleotide at each position to report the average SHAP value. The same procedure was used to determine the top Faith-Shap interactions (see Table S3), but instead by calculating the average contribution of each unique interaction. Total runtime was computed by summing the sample and computational complexities of each algorithm. We estimated the runtime per sample by dividing the total runtime by the number of query explanations performed.

To visualize SHAP values (see Fig. 2c and Fig. S3a), we randomly sampled 50 sequences and plotted their SHAP values on a scatterplot. To plot a histogram of Faith-Shap interactions (see Fig. 2e), we used the visualization scheme described in [23]. After separating the positive and negative interactions, we evenly distributed the interaction magnitudes across all affected nucleotides. We reported the summed contributions of each nucleotide at each position on a bar graph. However, slightly deviating from [23], rather than stratifying the bar plots by the order of interactions, we stratified them by nucleotide type and only plot interactions with an order greater than 1. For more details, refer to Appendix B of [23]. To visualize Faith-Shap interactions as shown in the Supplementary Material (see Fig. S1), we plotted interactions as data points with line connecting points to show the order of interaction. For visual clarity, we only plotted the larger interaction if interactions with the same nucleotides at the same positions have an estimated difference of 0.001. We plotted the top 80 interactions from SHAP zero and SHAP-IQ.

Experimental setup: inDelphi. We applied SHAP zero on inDelphi by inputting $n = 40$ DNA target sequences, which were additionally padded with 20 nucleotides on each end due to inDelphi’s minimum length requirement, to get their frameshift frequency. We used the same recommended q -SFT

parameters as in the TIGER experiment. The procedure to find hyperparameters b and $noise_sd$ was also the same, except that we refined our $noise_sd$ using a step size of 0.1. We used $b = 7$ and $noise_sd = 15$, which corresponded to an R^2 of 0.82.

We used the held-out DNA target sequences provided by inDelphi [33] to predict the experimental scores, which are available as a CSV file on our GitHub. We evaluated the performance of the recovered Fourier coefficients using Pearson and Spearman correlation. Since inDelphi does not have an option to threshold predictions like in TIGER, we do not report AUROC or AUPRC. The baseline models were trained on one-hot encoded sequences using the training data from inDelphi to predict inDelphi’s predicted frameshift frequency, as the experimental frameshift frequencies were not provided. KernelSHAP, SHAP-IQ, and FastSHAP were created using the same procedure as in the TIGER experiment. We were not able to run DeepSHAP on inDelphi, as inDelphi uses scikit-learn to train its models, which is not compatible with the SHAP package.

SHAP zero was run on all held-out sequences plus an additional 50 training sequences due to the limited amounts of held-out data to compute SHAP values and Faith-Shap interactions. We created the KernelSHAP and Faith-Shap baselines following the procedure outlined in the TIGER experiment. Due to computational issues with SHAP-IQ, we randomly selected four sequences to analyze. We ran KernelSHAP and Faith-Shap with a background dataset of 30 samples randomly drawn from the training set, separate from the 50 training sequences used for analysis. We used $max_order = 3$ and $budget = 20,000$ for SHAP-IQ. Top SHAP values (see Table S4 and Table S5), top Faith-Shap interactions (see Table S6), total runtime, and visualization schemes (see Fig. 3c, Fig. 3e, Fig. S2, and Fig. S4a) were computed similarly to those in the TIGER experiment.

Background and notation. We consider the problem of explaining a black-box model $f(\mathbf{x}) : \mathbb{Z}_q^n \rightarrow \mathbb{R}$ which maps from the space \mathbb{Z}_q^n (i.e., n -dimensional ring of integers modulo q [28]) to a real number. Hereafter, we will use bold lowercase (e.g. \mathbf{x}) to denote vectors. We denote $[n] = \{1, 2, 3, \dots, n\}$ and the vector $\mathbf{x} \in \mathbb{Z}_q^n$ as the q -ary representation of $\mathbf{x} = [x_1, \dots, x_n]^T \in \mathbb{Z}_q^n$. We also denote a subset of d coordinates $T = \{t_1, \dots, t_d\} \subset [n]$ to index over the input vector $\mathbf{x}_T = [x_{t_1}, \dots, x_{t_d}]$, where x_{t_i} is the value of the t_i -th coordinate in the vector \mathbf{x} .

SHAP values aim to explain the prediction of an input vector \mathbf{x} by assigning importance to each feature, where the value function $v_T(\mathbf{x})$ quantifies how much the features in T contribute toward the prediction of $f(\mathbf{x})$. Although there are many ways to compute the value function, one popular method is to marginalize all the features not in T , which we will refer to as \bar{T} [7]. More specifically, \bar{T} is the complement of T ($\bar{T} = D \setminus T$) and $T \cup \bar{T} = D$. With this, we can define the value function as the expectation of $f(\mathbf{x})$ with respect to $\mathbf{x}_{\bar{T}}$:

$$v_T(\mathbf{x}) = \mathbb{E}_{p(\mathbf{x}_{\bar{T}})} [f(\mathbf{x})] \tag{3}$$

Here, we take the expectation over the marginal distribution $p(\mathbf{x}_{\bar{T}})$ for the missing inputs. Equation (3) can be computed for any Shapley problem by approximating the missing inputs $\mathbf{x}_{\bar{T}}$. However, over a q -ary alphabet, we can compute this equation exactly because we know that every possible missing input must be in the space $\mathbb{Z}_q^{\bar{T}}$. If we assume that each permutation of $\mathbf{x}_{\bar{T}}$ is equally likely, the value

function reduces to taking an average contribution over $q^{|\bar{T}|}$ possible inputs:

$$v_T(\mathbf{x}) = \frac{1}{q^{|\bar{T}|}} \sum_{\substack{\mathbf{m}: \mathbf{m}_{\bar{T}} \in \mathbb{Z}_q^{|\bar{T}|} \\ \mathbf{m}_T = \mathbf{x}_T}} f(\mathbf{m}). \quad (4)$$

Background on sparse Fourier transforms. The key to SHAP zero lies in the assumption that the model is s -sparse in the Fourier domain. We leverage subsampling of the input sequence using patterns from sparse-graph codes [28]. This subsampling leads to a linear mixing of Fourier coefficients, allowing us to apply a peeling-decoding algorithm on the sparse-graph code to efficiently recover the top Fourier coefficients with $\mathcal{O}(sn^2)$ sample and $\mathcal{O}(sn^3)$ runtime complexity [28].

Let $\omega = e^{\frac{2\pi j}{q}}$. We can write out $f : \mathbb{Z}_q^n \rightarrow \mathbb{R}$ in terms of its Fourier transform $F[\mathbf{y}]$, where \mathbf{y} is the frequency vector:

$$f(\mathbf{m}) = \sum_{\mathbf{y} \in \mathbb{Z}_q^n} F[\mathbf{y}] \omega^{\langle \mathbf{m}, \mathbf{y} \rangle}, \quad \mathbf{m} \in \mathbb{Z}_q^n. \quad (5)$$

For instance, if we observe the functional landscape $f(\mathbf{m}) = (5 + 2j)\omega^{\langle \mathbf{m}, [0, 1, 0] \rangle} - (3 + j)\omega^{\langle \mathbf{m}, [1, 2, 0] \rangle} + (1 + j)\omega^{\langle \mathbf{m}, [1, 0, 3] \rangle}$ defined over $n = 3$ sites for a $q = 4$ alphabet, then we can note that f contains the Fourier coefficients $F[[0, 1, 0]] = 5 + 2j$, $F[[1, 2, 0]] = -(3 + j)$, and $F[[1, 0, 3]] = 1 + j$. The Fourier transform is sparse with $s = 3$ non-zero coefficients out of $4^3 = 64$ coefficients.

Overview of the Möbius transform. SHAP zero relies on converting hashed Fourier coefficients into the Möbius transform, which can then be converted into SHAP values and interactions. The Möbius transform marginalizes the contributions between interactions of sets [30]. However, the Fourier coefficients SHAP zero recovers are expressed as q -ary vectors, not as sets. For this reason, we will first introduce the classic Möbius transform formulation, which we will refer to as the set Möbius transform for clarity, and introduce the SHAP equation in terms of the set Möbius transform. Then, we will introduce a q -ary extension of the set Möbius transform, which is what SHAP zero uses. The definition of the set Möbius transform is as follows.

Definition 9.1. (*Set Möbius transform*). Given a value function $v : 2^n \rightarrow \mathbb{R}$ and a set S , the set Möbius transform $a(v, S)$ is defined as

$$a(v, S) = \sum_{T \subseteq S} (-1)^{|S| - |T|} v_T(\mathbf{x}), \quad (6)$$

with its inverse being defined as

$$v_T(\mathbf{x}) = \sum_{S \subseteq T} a(v, S). \quad (7)$$

For a full derivation of the set Möbius transform, see pages 344 to 347 of [31]. Each set Möbius transform coefficient $a(v, S)$, where $S \subseteq T$, represents the marginal contribution of the subset S , given

a value function v , in determining the score $v_T(\mathbf{x})$. Reconstructing the original score $v_T(\mathbf{x})$ from all subsets $S \subseteq T$ requires taking a linear sum over all the marginal contributions. For instance, in an $n = 3$ problem, say we want to compute the set Möbius transform of the set $S = \{1, 3\}$. Let \emptyset refer to the empty set, and let $v_\emptyset(\mathbf{x})$ be the output of the value function v when no inputs are given. The set Möbius transform $a(v, S)$ can be written as

$$a(v, \{1, 3\}) = (-1)^{|\{1,3\}|-|\{1,3\}|}v_{\{1,3\}}(\mathbf{x}) + (-1)^{|\{1,3\}|-|\{1\}|}v_{\{1\}}(\mathbf{x}) \\ + (-1)^{|\{1,3\}|-|\{3\}|}v_{\{3\}}(\mathbf{x}) + (-1)^{|\{1,3\}|-|\emptyset|}v_\emptyset(\mathbf{x}).$$

Each exponent raised to the negative one corresponds to the sign of each value function's output. Simplifying each exponent results in the following:

$$a(v, \{1, 3\}) = v_{\{1,3\}}(\mathbf{x}) - v_{\{1\}}(\mathbf{x}) - v_{\{3\}}(\mathbf{x}) + v_\emptyset(\mathbf{x}).$$

Now, suppose we want to compute the inverse set Möbius transform of the set $T = \{1, 3\}$. The value function can be written in terms of $a(v, S)$:

$$v_{\{1,3\}}(\mathbf{x}) = a(v, \emptyset) + a(v, \{1\}) + a(v, \{3\}) + a(v, \{1, 3\}).$$

Ultimately, we require a q -ary extension of the Möbius transform to work in a q -ary alphabet. We will introduce the q -ary Möbius transform in terms of vector notation and then later derive the conversion from the q -ary Möbius transform to the set Möbius transform.

We extend the q -ary Möbius transform from the vectorized Möbius transform found in [42]. The vectorized Möbius transform is characterized in $f : \mathbb{Z}_2^n \rightarrow \mathbb{R}$, whereas the q -ary Möbius transform is characterized in $f : \mathbb{Z}_q^n \rightarrow \mathbb{R}$. Notably, the q -ary Möbius transform works directly on f , rather than through a value function. Therefore, converting the q -ary Möbius transform to SHAP values first requires a conversion from the q -ary Möbius transform to the value function, which we will detail in a later section.

Extending the vectorized Möbius transform into the q -ary domain involves generalizing standard real field operations from $f : \mathbb{Z}_2^n \rightarrow \mathbb{R}$ to $f : \mathbb{Z}_q^n \rightarrow \mathbb{R}$. We define subtraction of $\mathbf{k} - \mathbf{m}$ by standard real field subtraction over \mathbb{Z}_q^n . To illustrate this, consider the vectors $\mathbf{k} = [1, 0, 2]$ and $\mathbf{m} = [1, 0, 0]$. Then,

$$\|\mathbf{k} - \mathbf{m}\|_0 = \|[1, 0, 2] - [1, 0, 0]\|_0 = \|[0, 0, 2]\|_0 = 1.$$

Standard real field subtraction over \mathbb{Z}_q^n is only computable when $\mathbf{m} \leq \mathbf{k}$. We define $\mathbf{m} \leq \mathbf{k}$ to be $m_i = k_i$ or $m_i = 0$ for all of i . For example, the vectors $\mathbf{m} = [1, 0, 0]$ and $\mathbf{k} = [1, 0, 2]$ satisfy $\mathbf{m} \leq \mathbf{k}$: $m_1 = k_1 = 1$, $m_2 = k_2 = 0$, and $m_3 = 0$. An example of vectors that do not satisfy $\mathbf{m} \leq \mathbf{k}$ are $\mathbf{m} = [1, 1, 1]$ and $\mathbf{k} = [1, 0, 2]$. Here, $m_2 = 1 \neq k_2 = 0$ and $m_3 = 1 \neq k_3 = 2$, so $\mathbf{m} \leq \mathbf{k}$ is violated. Using standard real field operations, the q -ary Möbius transform can be defined as follows.

Definition 9.2. (*q-ary Möbius transform*). Given $f : \mathbb{Z}_q^n \rightarrow \mathbb{R}$, the *q-ary Möbius transform* $M[\mathbf{k}]$, where \mathbf{k} is the feature interaction vector, can be defined as

$$M[\mathbf{k}] = \sum_{\mathbf{m} \leq \mathbf{k}} (-1)^{\|\mathbf{k}-\mathbf{m}\|_0} f(\mathbf{m}), \quad \mathbf{m} \in \mathbb{Z}_q^n, \quad \mathbf{k} \in \mathbb{Z}_q^n, \quad (8)$$

with its inverse being defined as

$$f(\mathbf{m}) = \sum_{\mathbf{k} \leq \mathbf{m}} M[\mathbf{k}]. \quad (9)$$

For instance, in a $q = 3$ and $n = 3$ problem, computing $M[\mathbf{k}]$ for the vector $\mathbf{k} = [1, 0, 2]$ can be written as

$$\begin{aligned} M[[1, 0, 2]] &= (-1)^{\|[1,0,2]-[1,0,2]\|_0} f([1, 0, 2]) + (-1)^{\|[1,0,2]-[1,0,0]\|_0} f([1, 0, 0]) \\ &\quad + (-1)^{\|[1,0,2]-[0,0,2]\|_0} f([0, 0, 2]) + (-1)^{\|[1,0,2]-[0,0,0]\|_0} f([0, 0, 0]). \end{aligned}$$

Similar to the set Möbius transform, the *q-ary Möbius transform* also raises an exponent to the negative one, which denotes the sign of each function f 's output. Simplifying each exponent results in the following:

$$M[[1, 0, 2]] = f([1, 0, 2]) - f([1, 0, 0]) - f([0, 0, 2]) + f([0, 0, 0]).$$

Now, suppose we want to compute the inverse *q-ary Möbius transform* to get $f(\mathbf{m})$ for the vector $\mathbf{m} = [1, 0, 2]$. $f([1, 0, 2])$ can be written as the following:

$$f([1, 0, 2]) = M[[0, 0, 0]] + M[[1, 0, 0]] + M[[0, 0, 2]] + M[[1, 0, 2]].$$

Finding *q-ary Möbius coefficients from the sparse Fourier transform.* In the *q-ary Fourier transform*, all alphabets in q are treated as a dictionary that maps an input to a *q-ary value* [28]. SHAP zero uses this encoding pattern to compute the *q-ary Fourier transform*. Let $\mathbf{0}_n$ be the all 0's vector of length n . To simplify the derivation and computation of Shapley-based explanations, for each input query sequence \mathbf{x} , we shift the encoding pattern of \mathbf{x} to $\hat{\mathbf{x}}$ and the Fourier coefficients $F[\mathbf{y}]$ to $\hat{F}[\mathbf{y}]$ such that $\hat{\mathbf{x}} = \mathbf{0}_n$ and:

$$f(\mathbf{x}) = \sum_{\mathbf{y} \in \mathbb{Z}_q^n} F[\mathbf{y}] \omega^{\langle \mathbf{x}, \mathbf{y} \rangle} = \sum_{\mathbf{y} \in \mathbb{Z}_q^n} \hat{F}[\mathbf{y}] \omega^{\langle \hat{\mathbf{x}}, \mathbf{y} \rangle} = \sum_{\mathbf{y} \in \mathbb{Z}_q^n} \hat{F}[\mathbf{y}]. \quad (10)$$

For example, given a $q = 4$ and $n = 3$ problem, the model expects a DNA sequence of length three as an input. In the *q-ary Fourier transform*, the input query sequence 'ACG' gets encoded into $[0, 1, 2]$, assuming the dictionary pattern where $0 = \text{A}$, $1 = \text{C}$, $2 = \text{G}$, and $3 = \text{T}$. However, we would like this exact sequence to get encoded as $[0, 0, 0]$, since 'ACG' is the input query sequence being explained.

To shift the Fourier coefficients properly to satisfy Equation (10), [28] states that every Fourier coefficient must be shifted by the sample's *q-ary encoding* using the following equation:

$$\hat{F}[\mathbf{y}] = F[\mathbf{y}] \omega^{\langle \mathbf{x}, \mathbf{y} \rangle}, \quad (11)$$

where $\hat{F}[\mathbf{y}]$ refers to the shifted Fourier coefficient, \mathbf{x} refers to the Fourier-encoded query sequence, and $F[\mathbf{y}]$ refers to the original q -ary Fourier coefficient. To shift the entire s -sparse Fourier transform, we have to loop over all s Fourier coefficients and shift them by the query sequence.

After shifting all s Fourier coefficients using Equation (11), we plug in Equation (5) into Equation (8) to obtain:

$$M_{\mathbf{x}}[\mathbf{k}] = \sum_{\mathbf{m} \leq \mathbf{k}} (-1)^{\|\mathbf{k}-\mathbf{m}\|_0} \left(\sum_{\mathbf{y} \in \mathbb{Z}_q^n} \hat{F}[\mathbf{y}] \omega^{\langle \mathbf{m}, \mathbf{y} \rangle} \right), \quad (12)$$

where we now add the subscript \mathbf{x} in $M_{\mathbf{x}}[\mathbf{k}]$ to denote the q -ary Möbius transform after shifting the Fourier coefficients around \mathbf{x} . By pulling $\sum_{\mathbf{y} \in \mathbb{Z}_q^n} \hat{F}[\mathbf{y}]$ out of the summation $\sum_{\mathbf{m} \leq \mathbf{k}} (-1)^{\|\mathbf{k}-\mathbf{m}\|_0}$, we obtain the mapping from the q -ary Fourier transform to $M_{\mathbf{x}}[\mathbf{k}]$:

$$M_{\mathbf{x}}[\mathbf{k}] = \sum_{\mathbf{y} \in \mathbb{Z}_q^n} \hat{F}[\mathbf{y}] \left(\sum_{\mathbf{m} \leq \mathbf{k}} (-1)^{\|\mathbf{k}-\mathbf{m}\|_0} \omega^{\langle \mathbf{m}, \mathbf{y} \rangle} \right). \quad (13)$$

Equation (13) details how to convert the shifted Fourier transform to $M_{\mathbf{x}}[\mathbf{k}]$ for a single \mathbf{k} (a single q -ary Möbius coefficient). If no assumptions are made, the complexity of mapping the Fourier transform into every possible $M_{\mathbf{x}}[\mathbf{k}]$ scales with $\mathcal{O}(q^n)$. However, if we assume the Fourier transform is low-order and has a maximum order of ℓ , we can bound the number of nonzero elements in $M_{\mathbf{x}}[\mathbf{k}]$. This is because Equation (13) will always go to zero when there exists an i such that $y_i = 0$ and $k_i \neq 0$. As an example, consider finding the Möbius transform of a model which is $s = 1$ -sparse in Fourier and let us assume $\hat{F}[[2, 1, 0]]$ is the only non-zero Fourier coefficient. In this setup, one example of \mathbf{k} for which $M_{\mathbf{x}}[\mathbf{k}]$ is zero is $\mathbf{k} = [0, 1, 1]$ since it satisfies the condition that $y_3 = 0$ and $k_3 \neq 0$. Computing Equation (13), we get:

$$M_{\mathbf{x}}[\mathbf{k}] = \hat{F}[[2, 1, 0]] \left((-1)^{\|[0,1,1]-[0,0,0]\|_0} \omega^{\langle [0,0,0],[2,1,0] \rangle} + (-1)^{\|[0,1,1]-[0,1,0]\|_0} \omega^{\langle [0,1,0],[2,1,0] \rangle} \right. \\ \left. + (-1)^{\|[0,1,1]-[0,0,1]\|_0} \omega^{\langle [0,0,1],[2,1,0] \rangle} + (-1)^{\|[0,1,1]-[0,1,1]\|_0} \omega^{\langle [0,1,1],[2,1,0] \rangle} \right).$$

From here, we can simplify to the following:

$$M_{\mathbf{x}}[\mathbf{k}] = \hat{F}[[2, 1, 0]] \left((-1)^2 \omega^0 + (-1)^1 \omega^1 + (-1)^1 \omega^0 + (-1)^0 \omega^1 \right) = 0.$$

As a consequence, now we can bound the number of nonzero elements in $M_{\mathbf{x}}[\mathbf{k}]$ by counting the number of vectors \mathbf{k} for which there is no i such that $y_i = 0$ and $k_i \neq 0$. If we assume that the Fourier transform is low-order and bounded by ℓ , then we can bound it by $\mathcal{O}(q^\ell)$ instead of $\mathcal{O}(q^n)$.

Generalizing this example, if there exists an i such that $y_i = 0$ and $k_i \neq 0$, this allows us to rewrite Equation (13) as the following:

$$M_{\mathbf{x}}[\mathbf{k}] = \sum_{\mathbf{y} \in \mathbb{Z}_q^n} \hat{F}[\mathbf{y}] \left(\sum_{\substack{\mathbf{m} \leq \mathbf{k} \\ m_i = 0}} (-1)^{\|\mathbf{k}-\mathbf{m}\|_0} \omega^{\langle \mathbf{m}, \mathbf{y} \rangle} + (-1)^{\|\mathbf{k}-\mathbf{m}^+\|_0} \omega^{\langle \mathbf{m}^+, \mathbf{y} \rangle} \right),$$

where \mathbf{m}^+ is equal to \mathbf{m} everywhere except at location i and $\mathbf{m}^+_i = k_i$. Since $y_i = 0$, $\langle \mathbf{m}, \mathbf{y} \rangle = \langle \mathbf{m}^+, \mathbf{y} \rangle$. Additionally, we can rewrite $\|\mathbf{k} - \mathbf{m}\|_0$ as $\|\mathbf{k} - \mathbf{m}^+\|_0 + 1$, since we know that the only difference between \mathbf{m}^+ and \mathbf{m} is a single nonzero value at position i . Therefore, we can say that:

$$M_{\mathbf{x}}[\mathbf{k}] = \sum_{\mathbf{y} \in \mathbb{Z}_q^n} \hat{F}[\mathbf{y}] \left(\sum_{\substack{\mathbf{m} \leq \mathbf{k} \\ m_i = 0}} (-1)^{\|\mathbf{k}-\mathbf{m}\|_0} \omega^{\langle \mathbf{m}, \mathbf{y} \rangle} + (-1)^{\|\mathbf{k}-\mathbf{m}\|_0+1} \omega^{\langle \mathbf{m}, \mathbf{y} \rangle} \right) = 0.$$

We now move to analyze the computational complexity of converting from the Fourier to the q -ary Möbius transform. First, shifting all the Fourier coefficients scales with $\mathcal{O}(s)$, since we have to loop through all s Fourier coefficients once. The time complexity of doing the conversion using Equation (13) depends on the distribution of the Fourier coefficient interaction orders. In the worst-case scenario, we can assume that all Fourier coefficients are all ℓ -th order. We break up the problem into two categories: the computational complexity of computing the most expensive Möbius coefficient and analyzing the total amount of Möbius coefficients created. From Equation (13), the most expensive Möbius coefficient to compute will be an ℓ -th order Möbius coefficient due to summing over 2^ℓ vectors, which is the total amount of vectors encompassed in $\mathbf{m} \leq \mathbf{k}$; this single Möbius coefficient requires s summations over 2^ℓ vectors, which scales with computational complexity $\mathcal{O}(s2^\ell)$. Additionally, if all s Fourier coefficients are ℓ -th order, there are at most sq^ℓ possible q -ary Möbius coefficients to loop through. Therefore, the overall computational complexity of converting from the Fourier to the q -ary Möbius transform is $\mathcal{O}(s + s2^\ell \times sq^\ell) \approx \mathcal{O}(s^2(2q)^\ell)$.

Computing SHAP values from the q -ary Möbius transform. Here, we derive the following Theorem:

Theorem 9.1. (*q -ary Möbius transform to SHAP values*). Given the q -ary Möbius transform over the function $f : \mathbb{Z}_q^n \rightarrow \mathbb{R}$, the SHAP value equation can be written as

$$I^{SV}(i) = - \sum_{\bar{L} \subseteq D \setminus \{i\}} \frac{1}{|\bar{L} \cup \{i\}| q^{|\bar{L} \cup \{i\}|}} \sum_{\substack{\mathbf{m}: \forall j \in \bar{L} \cup \{i\}, m_j > 0 \\ \mathbf{m}_{L \setminus \{i\}} = \mathbf{0}_{L \setminus \{i\}}}} M_{\mathbf{x}}[\mathbf{m}], \quad (14)$$

or equivalently in vector notation as

$$I^{SV}(i) = - \sum_{\mathbf{k}: k_i > 0} \frac{1}{\|\mathbf{k}\|_0 q^{\|\mathbf{k}\|_0}} M_{\mathbf{x}}[\mathbf{k}], \quad (15)$$

with a computational complexity of $\mathcal{O}(q^\ell)$, where ℓ is the maximum order of the q -ary Möbius coefficients.

The remainder of this section will be dedicated to a full proof. Briefly, the steps involve finding a relationship between the set Möbius transform and the SHAP value and then converting the q -ary Möbius transform to the set Möbius transform.

We first explain the connection between the set Möbius transform and SHAP values. Plugging in Equation (7) into Equation (1) represents the SHAP value formula in terms of the set Möbius transform:

$$I^{SV}(i) = \sum_{T \subseteq D \setminus \{i\}} \frac{|T|!(|D| - |T| - 1)!}{|D|!} \left[\sum_{S \subseteq T \cup \{i\}} a(v, S) - \sum_{S \subseteq T} a(v, S) \right]. \quad (16)$$

Following the proof given in [30], simplifying this equation results in the final representation, which we give below.

Definition 9.3. (*SHAP values in terms of the set Möbius transform*). Given the set Möbius transform $a(v, S)$, the SHAP value equation can be written as

$$I^{SV}(i) = \sum_{T \subseteq D \setminus \{i\}} \frac{1}{|T \cup \{i\}|} a(v, T \cup \{i\}). \quad (17)$$

Computing SHAP values from the q -ary Möbius transform first requires a conversion from the q -ary to set Möbius transform. We plug in Equation (10) into the value function from Equation (4) in order to use the shifted Fourier coefficients. By using $\hat{F}[\mathbf{k}]$, this means that $\mathbf{m}_T = \hat{\mathbf{x}}_T = \mathbf{0}_{|T|}$.

$$v_T(\mathbf{x}) = \frac{1}{q^{|\bar{T}|}} \sum_{\substack{\mathbf{m}: \mathbf{m}_{\bar{T}} \in \mathbb{Z}_q^{|\bar{T}|} \\ \mathbf{m}_T = \mathbf{x}_T}} f(\mathbf{m}) = \frac{1}{q^{|\bar{T}|}} \sum_{\substack{\mathbf{m}: \mathbf{m}_{\bar{T}} \in \mathbb{Z}_q^{|\bar{T}|} \\ \mathbf{m}_T = \mathbf{0}_{|T|}}} \left(\sum_{\mathbf{y} \in \mathbb{Z}_q^n} \hat{F}[\mathbf{y}] \omega^{\langle \mathbf{m}, \mathbf{y} \rangle} \right). \quad (18)$$

Then, we plug in the inverse q -ary Möbius transform from Equation (9) into Equation (18):

$$v_T(\mathbf{x}) = \frac{1}{q^{|\bar{T}|}} \sum_{\substack{\mathbf{m}: \mathbf{m}_{\bar{T}} \in \mathbb{Z}_q^{|\bar{T}|} \\ \mathbf{m}_T = \mathbf{0}_{|T|}}} \left(\sum_{\mathbf{k} \leq \mathbf{m}} M_{\mathbf{x}}[\mathbf{k}] \right). \quad (19)$$

The value 0 is assigned to the subset indices T , which indexes the subset of the original inputs \mathbf{x}_T . Over the missing inputs $\mathbf{x}_{\bar{T}}$ and their indices \bar{T} , the vector $\mathbf{m}_{\bar{T}} \in \mathbb{Z}_q^{|\bar{T}|}$ is used. Due to the recursive nature of the q -ary Möbius transform, each q -ary Möbius coefficient is looped through $q^{|\bar{T}| - \|\mathbf{m}\|_0}$ times. Therefore, we can simplify Equation (19) as follows:

$$v_T(\mathbf{x}) = \frac{1}{q^{|\bar{T}|}} \sum_{\substack{\mathbf{m}: \mathbf{m}_{\bar{T}} \in \mathbb{Z}_q^{|\bar{T}|} \\ \mathbf{m}_T = \mathbf{0}_{|T|}}} q^{|\bar{T}| - \|\mathbf{m}\|_0} M_{\mathbf{x}}[\mathbf{m}]. \quad (20)$$

To simplify, we can pull the $q^{|\bar{T}|}$ out of the summation, which will allow us to cancel the $q^{|\bar{T}|}$ term in the denominator. This leaves us with the following:

$$v_T(\mathbf{x}) = \sum_{\substack{\mathbf{m}: \mathbf{m}_{\bar{T}} \in \mathbb{Z}_q^{|\bar{T}|} \\ \mathbf{m}_T = \mathbf{0}_{|T|}}} \frac{1}{q^{|\mathbf{m}|_0}} M_{\mathbf{x}}[\mathbf{m}]. \quad (21)$$

Plugging Equation (21) into the set Möbius transform equation from Equation (6) returns an equation for the set Möbius transform in terms of the q -ary Möbius transform:

$$a(v, S) = \sum_{T \subseteq S} \left((-1)^{|S|-|T|} \sum_{\substack{\mathbf{m}: \mathbf{m}_{\bar{T}} \in \mathbb{Z}_q^{|\bar{T}|} \\ \mathbf{m}_T = \mathbf{0}_{|T|}}} \frac{1}{q^{|\mathbf{m}|_0}} M_{\mathbf{x}}[\mathbf{m}] \right). \quad (22)$$

Although Equation (22) loops only over subsets $T \subseteq S$, all possible q -ary Möbius coefficients are accounted for, since \mathbf{m} is nonzero at coordinates given by \bar{T} . We rewrite Equation (22) such that we loop over all possible q -ary Möbius coefficients, given by the subsets $\bar{L} \subseteq D$:

$$a(v, S) = \sum_{\bar{L} \subseteq D} \left(\sum_{\substack{T: T \subseteq S \\ \text{if } \bar{L} \subseteq \bar{T}}} (-1)^{|S|-|T|} \left(\frac{1}{q^{|\bar{L}|}} \sum_{\substack{\mathbf{m}: \forall i \in \bar{L}, m_i > 0 \\ \mathbf{m}_L = \mathbf{0}_{|L|}}} M_{\mathbf{x}}[\mathbf{m}] \right) \right). \quad (23)$$

Notably, we are looping through $T \subseteq S$ over the set T in order to compute $(-1)^{|S|-|T|}$, but our if condition is with respect to \bar{T} . For every T , \bar{T} is implicitly defined already, since \bar{T} is the complement of T .

We look to simplify the outer summation. Consider the relationship between an arbitrary \bar{L} given the condition $\bar{L} \subseteq \bar{T}$. $\bar{L} \subseteq \bar{T}$ is only true when $\bar{L} \cap T = \emptyset$ based on the way \bar{T} is implicitly defined. Since $T \subseteq S$, the total number of features that can be in T that can satisfy $\bar{L} \cap T = \emptyset$ is $|S \setminus \bar{L}|$. Therefore, the amount of T subsets that will loop through $T \subseteq S$ is equal to $2^{|S \setminus \bar{L}|}$ for an arbitrary \bar{L} . From here, we will cancel out terms by noting that we must loop through the alternating series $2^{|S \setminus \bar{L}|}$ times. We divide \bar{L} into two cases: when $S \subseteq \bar{L}$ and when $S \not\subseteq \bar{L}$. When $S \not\subseteq \bar{L}$, $|S \setminus \bar{L}| > 0$, which means we loop through the alternating series an even amount of times, canceling out any q -ary Möbius coefficients that have $|\bar{L}|$ nonzero values. However, when $S \subseteq \bar{L}$, $|S \setminus \bar{L}| = 0$. Therefore, we can rewrite the outer summation to be over all possible \bar{L} 's where $S \subseteq \bar{L}$:

$$a(v, S) = \sum_{\bar{L}: S \subseteq \bar{L}} \left(\sum_{\substack{T: T \subseteq S \\ \text{if } \bar{L} \cap T = \emptyset}} (-1)^{|S|-|T|} \left(\frac{1}{q^{|\bar{L}|}} \sum_{\substack{\mathbf{m}: \forall i \in \bar{L}, m_i > 0 \\ \mathbf{m}_L = \mathbf{0}_{|L|}}} M_{\mathbf{x}}[\mathbf{m}] \right) \right). \quad (24)$$

Now, given $S \subseteq \bar{L}$, the only way $T \subseteq S$ and $\bar{L} \cap T = \emptyset$ can be satisfied is when $T = \emptyset$. T cannot contain any features in its set because it will violate $\bar{L} \cap T = \emptyset$. To illustrate this, consider an $n = 3$

problem. Let $S = \{1, 2\}$ and $\bar{L} = \{1, 2, 3\}$. The possible subsets $T \subseteq S$ include \emptyset , $\{1\}$, $\{2\}$, and $\{1, 2\}$. For the subsets $\{1\}$ and $\{2\}$, $\{1\} \cap \{1, 2, 3\} = \{1\} \neq \emptyset$ and $\{2\} \cap \{1, 2, 3\} = \{2\} \neq \emptyset$. The only case where $\bar{L} \cap T = \emptyset$ is when $T = \emptyset$, which means $|T| = 0$.

Setting $|T| = 0$ and the outer summation to loop over all possible \bar{L} 's where $S \subseteq \bar{L}$, we obtain the following expression:

$$a(v, S) = \sum_{\bar{L}: S \subseteq \bar{L}} \left((-1)^{|S|} \left(\frac{1}{q^{|\bar{L}|}} \sum_{\substack{\mathbf{m}: \forall i \in \bar{L}, m_i > 0 \\ \mathbf{m}_L = \mathbf{0}_{|L|}}} M_{\mathbf{x}}[\mathbf{m}] \right) \right). \quad (25)$$

Pulling $(-1)^{|S|}$ out of the summation, we obtain an expression to convert from the q -ary Möbius transform to set Möbius transform.

Theorem 9.2. (*Conversion from q -ary Möbius transform to set Möbius transform*). *The conversion from the q -ary Möbius transform over the function $f : \mathbb{Z}_q^n \rightarrow \mathbb{R}$ to the set Möbius transform $a(v, S)$ is*

$$a(v, S) = (-1)^{|S|} \sum_{\bar{L}: S \subseteq \bar{L}} \left(\frac{1}{q^{|\bar{L}|}} \sum_{\substack{\mathbf{m}: \forall i \in \bar{L}, m_i > 0 \\ \mathbf{m}_L = \mathbf{0}_{|L|}}} M_{\mathbf{x}}[\mathbf{m}] \right), \quad (26)$$

or equivalently in vector notation as

$$a(v, S) = (-1)^{|S|} \sum_{\mathbf{k}: \mathbf{k}_S > \mathbf{0}_{|S|}} \frac{1}{q^{||\mathbf{k}||_0}} M_{\mathbf{x}}[\mathbf{k}]. \quad (27)$$

With a conversion from the q -ary Möbius transform to the set Möbius transform, we can now derive the SHAP value formula with respect to the q -ary Möbius transform. To do this, we will need to use the following lemmas.

Lemma 9.3. *For all $n \geq 0$ and $k \geq 0$, where n and k are integers:*

$$\binom{n-1}{k-1} = \frac{k}{n} \binom{n}{k}.$$

Proof. Expanding the right-hand side results in the following: $\binom{n-1}{k-1} = \frac{k}{n} \binom{n}{k} = \frac{k \cdot n!}{n \cdot k! \cdot (n-k)!} = \frac{(n-1)!}{(k-1)! \cdot (n-k)!} = \binom{n-1}{k-1}$. \square

Lemma 9.4. *For all $n \geq 1$, where n is an integer:*

$$\sum_{k=1}^n (-1)^k \binom{n}{k} = -1.$$

Proof. We require a special case of the binomial theorem. The binomial theorem states that, for any number x and y , and given an integer $n \geq 0$: $(x + y)^n = \sum_{k=0}^n \binom{n}{k} x^k y^{n-k}$. Plugging in $y = 1$ and $x = -1$ leads to the following simplification: $\sum_{k=0}^n (-1)^k \binom{n}{k} = 0$. We pull out the summation term where $k = 0$, and instead loop the summation over from $k = 1$ to n : $1 + \sum_{k=1}^n (-1)^k \binom{n}{k} = 0$. Finally, isolating the summation term leaves us with Lemma 9.4. $\sum_{k=1}^n (-1)^k \binom{n}{k} = -1$. \square

To begin our derivation, we plug in Equation (26) into Equation (17):

$$I^{SV}(i) = \sum_{T \subseteq D \setminus \{i\}} \frac{1}{|T \cup \{i\}|} \left((-1)^{|T \cup \{i\}|} \sum_{\bar{L}: T \cup \{i\} \subseteq \bar{L}} \left(\frac{1}{q^{|\bar{L}|}} \sum_{\substack{\mathbf{m}: \forall j \in \bar{L}, m_j > 0 \\ \mathbf{m}_L = \mathbf{0}_{|L|}} M_{\mathbf{x}}[\mathbf{m}] \right) \right). \quad (28)$$

Summing up over all sets $T \subseteq D \setminus \{i\}$ results in repeatedly looping over the same q -ary Möbius coefficients several times. We re-write Equation (28) to sum over all q -ary Möbius coefficient sets $\bar{L} \subseteq D \setminus \{i\}$, which allows us to loop over all unique q -ary Möbius coefficients as we keep track of how many times the alternating series gets summed:

$$I^{SV}(i) = \sum_{\bar{L} \subseteq D \setminus \{i\}} \frac{1}{q^{|\bar{L} \cup \{i\}|}} \left(\sum_{\substack{\mathbf{m}: \forall j \in \bar{L} \cup \{i\}, m_j > 0 \\ \mathbf{m}_{L \setminus \{i\}} = \mathbf{0}_{|L \setminus \{i\}|}} M_{\mathbf{x}}[\mathbf{m}] \left(\sum_{\substack{T \subseteq \bar{L} \cup \{i\} \\ i \in T}} \frac{1}{|T|} (-1)^{|T|} \right) \right). \quad (29)$$

The amount of times to sum through $\sum_{T \subseteq \bar{L} \cup \{i\}, i \in T} \frac{1}{|T|} (-1)^{|T|}$ depends on $|T|$. For example, consider $n = 3$ problem, where $i = 1$ and $\bar{L} = \{2, 3\}$. There is only one possible set where $|T| = 1$, $\{1\}$, because $i \in T$. However, there are two possible sets where $|T| = 2$: $\{1, 2\}$ and $\{1, 3\}$. Generalizing this, the amount of possible sets for an arbitrary $|T|$ that satisfy $i \in T$ is equivalent to $\binom{|\bar{L} \cup \{i\}| - 1}{|T| - 1}$. Using this, we re-write Equation (29) by summing over all possibilities of $|T|$:

$$I^{SV}(i) = \sum_{\bar{L} \subseteq D \setminus \{i\}} \frac{1}{q^{|\bar{L} \cup \{i\}|}} \left(\sum_{\substack{\mathbf{m}: \forall j \in \bar{L} \cup \{i\}, m_j > 0 \\ \mathbf{m}_{L \setminus \{i\}} = \mathbf{0}_{|L \setminus \{i\}|}} M_{\mathbf{x}}[\mathbf{m}] \left(\sum_{k=1}^{|\bar{L} \cup \{i\}|} \binom{|\bar{L} \cup \{i\}| - 1}{k - 1} \frac{1}{k} (-1)^k \right) \right). \quad (30)$$

We can apply Lemmas 9.3 and 9.4 to arrive at the following:

$$I^{SV}(i) = \sum_{\bar{L} \subseteq D \setminus \{i\}} \frac{1}{q^{|\bar{L} \cup \{i\}|}} \left(\sum_{\substack{\mathbf{m}: \forall j \in \bar{L} \cup \{i\}, m_j > 0 \\ \mathbf{m}_{L \setminus \{i\}} = \mathbf{0}_{|L \setminus \{i\}|}} M_{\mathbf{x}}[\mathbf{m}] \left(\frac{1}{|\bar{L} \cup \{i\}|} \sum_{k=1}^{|\bar{L} \cup \{i\}|} \binom{|\bar{L} \cup \{i\}|}{k} (-1)^k \right) \right). \quad (31)$$

$$I^{SV}(i) = \sum_{\bar{L} \subseteq D \setminus \{i\}} \frac{1}{q^{|\bar{L} \cup \{i\}|}} \left(\sum_{\substack{\mathbf{m}: \forall j \in \bar{L} \cup \{i\}, m_j > 0 \\ \mathbf{m}_{L \setminus \{i\}} = \mathbf{0}_{|L \setminus \{i\}|}} M_{\mathbf{x}}[\mathbf{m}] \left(\frac{-1}{|\bar{L} \cup \{i\}|} \right) \right). \quad (32)$$

Finally, we can pull $\frac{-1}{|\bar{L} \cup \{i\}|}$ out of the summation to be left with our final expression, as described in Equation (14):

$$I^{SV}(i) = - \sum_{\bar{L} \subseteq D \setminus \{i\}} \frac{1}{|\bar{L} \cup \{i\}| q^{|\bar{L} \cup \{i\}|}} \sum_{\substack{\mathbf{m}: \forall j \in \bar{L} \cup \{i\}, m_j > 0 \\ \mathbf{m}_{L \setminus \{i\}} = \mathbf{0}_{|L \setminus \{i\}|}}} M_{\mathbf{x}}[\mathbf{m}]. \quad (33)$$

This is equivalently written in vector notation as:

$$I^{SV}(i) = - \sum_{\mathbf{k}: k_i > 0} \frac{1}{\|\mathbf{k}\|_0 q^{\|\mathbf{k}\|_0}} M_{\mathbf{x}}[\mathbf{k}]. \quad (34)$$

Analyzing the time complexity, in the worst-case scenario, if every q -ary Möbius coefficient is nonzero up to order ℓ , the total amount of coefficients to sum up is $q^{\ell-1}(q-1) \approx q^\ell$. Therefore, the time complexity of Equation (34) is upper-bounded by $\mathcal{O}(q^\ell)$. We note that there might be more direct ways to map the Fourier transform to SHAP, such as simplifying our formulations and skipping the Möbius transform. However, we chose to make this connection concert due to the standard usage of the Möbius transform in SHAP.

Overview of Shapley interactions and Faith-Shap interactions. Extending Shapley values, which assign attributions to each feature, to interaction indices, which assign attributions to interactions of features, is an open-ended problem in explainability literature; the natural extensions of the axioms that govern Shapley values no longer guarantee a unique explanation [21]. As such, several interaction indices have been developed that add additional constraints to the original Shapley interaction extensions [21, 22, 43]. In this work, we choose to utilize the Faith-Shap interaction index to explain interactions, which has the additional property that the interactions are faithful to the value function: the sum of all possible feature interactions over a subset T should approximate $v_T(\mathbf{x})$ [21].

The Faith-Shap interaction index, which has a natural connection to the set Möbius transform equation, can be defined as follows:

Definition 9.4. (*Faith-Shap [21]*). *Given a maximum interaction order ℓ , the Faith-Shap interaction index over a set T , $I^{FSI}(T)$, can be written as:*

$$I^{FSI}(T) = a(v, T) + (-1)^{\ell-|T|} \frac{|T|}{\ell + |T|} \binom{\ell}{|T|} \sum_{\substack{S \supset T, \\ |S| > \ell}} \frac{\binom{|S|-1}{\ell}}{\binom{|S|+\ell-1}{\ell+|T|}} a(v, S), \quad \forall T \in T_\ell. \quad (35)$$

where T_ℓ denotes the set of all subsets T in D where $|T| \leq \ell$.

In practice, the maximum order of interaction ℓ to compute is determined by the user. For instance, in an $n = 4$ and $\ell = 2$ problem, the Faith-Shap interaction index of the set $\{1, 2\}$ can be written as

follows:

$$I^{FSI}(\{1, 2\}) = a(v, \{1, 2\}) + (-1)^{2-2} \frac{2}{2+2} \binom{2}{2} \left(\frac{\binom{3-1}{2}}{\binom{3+2-1}{2+2}} a(v, \{1, 2, 3\}) \right. \\ \left. + \frac{\binom{3-1}{2}}{\binom{3+2-1}{2+2}} a(v, \{1, 2, 4\}) + \frac{\binom{4-1}{2}}{\binom{4+2-1}{2+2}} a(v, \{1, 2, 3, 4\}) \right)$$

Equation (35) is not computationally scalable, as the set Möbius transform requires looping over $2^{|D|}$ subsets. However, for a q -ary Möbius transform with a maximum order ℓ , all set Möbius coefficients with a maximum order greater than ℓ are 0, by Equation (26). Therefore, when computing the ℓ^{th} order Faith-Shap interaction index, there are no set Möbius coefficients that satisfy $|T| > \ell$ in the summation term of Equation (35), allowing us to drop the summation term. Therefore, we can define the SHAP zero q -ary extension of the Faith-Shap interaction index as follows, where the equivalent vector statement comes from Theorem 9.2:

Theorem 9.5. (*q -ary Möbius transform to Faith-Shap*). *Given the q -ary Möbius transform over the function $f : \mathbb{Z}_q^n \rightarrow \mathbb{R}$ with a maximum order ℓ , the ℓ^{th} order Faith-Shap interaction index equation can be written as*

$$I^{FSI}(T) = a(v, T), \quad \forall T \in \mathcal{T}_\ell, \quad (36)$$

or equivalently in vector notation as

$$I^{FSI}(T) = (-1)^{|T|} \sum_{\mathbf{k}: \mathbf{k}_T > \mathbf{0}_{|T|}} \frac{1}{q^{|\mathbf{k}|_0}} M_{\mathbf{x}}[\mathbf{k}], \quad (37)$$

with a computational complexity of $\mathcal{O}(q^\ell)$.

Similarly to the computational complexity from Theorem 9.1, if every q -ary Möbius coefficient is nonzero up to order ℓ , the total amount of coefficients to sum up is $q^{\ell-|T|} (q-1)^{|T|} \approx q^\ell$. Therefore, the time complexity of Theorem 9.5 is $\mathcal{O}(q^\ell)$. Notably, when $\ell = 1$, Theorem 9.5 becomes identical to computing SHAP values in Theorem 9.1.

References

- [1] Lloyd S. Shapley. A value for n -person games. In *Contributions to the Theory of Games*, volume 2, pages 307–317. Princeton University Press, 1953.
- [2] Sara Hooker, Dumitru Erhan, Pieter-Jan Kindermans, and Been Kim. A benchmark for interpretability methods in deep neural networks. In *Advances in Neural Information Processing Systems*, volume 32, 2019.

- [3] Anupam Datta, Shayak Sen, and Yair Zick. Algorithmic transparency via quantitative input influence: Theory and experiments with learning systems. In *2016 IEEE Symposium on Security and Privacy (SP)*, pages 598–617. IEEE, 2016.
- [4] Guy Van den Broeck, Anton Lykov, Maximilian Schleich, and Dan Suci. On the tractability of SHAP explanations. In *Proceedings of the 35th Conference on Artificial Intelligence (AAAI)*, 2021.
- [5] Nicolae Sapoval, Amirali Aghazadeh, Michael G. Nute, Dinler A. Antunes, Advait Balaji, Richard Baraniuk, C. J. Barberan, Ruth Dannenfeler, Chen Dun, Mohammadamin Edrisi, R. A. Leo Elworth, Bryce Kille, Anastasios Kyrillidis, Luay Nakhleh, Cameron R. Wolfe, Zhi Yan, Vicky Yao, and Todd J. Treangen. Current progress and open challenges for applying deep learning across the biosciences. *Nature Communications*, 13(1):1728, 2022.
- [6] Scott M. Lundberg and Su-In Lee. A unified approach to interpreting model predictions. In *Advances in Neural Information Processing Systems*, volume 30, 2017.
- [7] Hugh Chen, Ian C. Covert, Scott M. Lundberg, and Su-In Lee. Algorithms to estimate Shapley value feature attributions. *Nature Machine Intelligence*, 5(6):590–601, 2023.
- [8] Erik Štrumbelj and Igor Kononenko. An efficient explanation of individual classifications using game theory. *The Journal of Machine Learning Research*, 11:1–18, 2010.
- [9] Javier Castro, Daniel Gómez, and Juan Tejada. Polynomial calculation of the Shapley value based on sampling. *Computers & Operations Research*, 36(5):1726–1730, 2009.
- [10] Grah Simon and Vincent Thouvenot. A projected stochastic gradient algorithm for estimating Shapley value applied in attribute importance. In *Proceedings of the International Cross-Domain Conference for Machine Learning and Knowledge Extraction*, pages 97–115. Springer International Publishing, 2020.
- [11] Erik Štrumbelj and Igor Kononenko. Explaining prediction models and individual predictions with feature contributions. *Knowledge and Information Systems*, 41:647–665, 2014.
- [12] Ian Covert, Scott M. Lundberg, and Su-In Lee. Understanding global feature contributions with additive importance measures. In *Advances in Neural Information Processing Systems*, volume 33, pages 17212–17223, 2020.
- [13] Avanti Shrikumar, Peyton Greenside, and Anshul Kundaje. Learning important features through propagating activation differences. In *International Conference on Machine Learning*, pages 3145–3153. PMLR, 2017.
- [14] Marco Ancona, Cengiz Oztireli, and Markus Gross. Explaining deep neural networks with a polynomial time algorithm for Shapley value approximation. In *International Conference on Machine Learning*, pages 272–281. PMLR, 2019.

- [15] Rui Wang, Xiaoqian Wang, and David I. Inouye. Shapley explanation networks. In *International Conference on Learning Representations*, 2021.
- [16] Hugh Chen, Scott M. Lundberg, and Su-In Lee. Explaining a series of models by propagating Shapley values. *Nature Communications*, 13(1):4512, 2022.
- [17] Jianbo Chen, Le Song, Martin J. Wainwright, and Michael I. Jordan. L-Shapley and C-Shapley: Efficient model interpretation for structured data. In *International Conference on Learning Representations*, 2019.
- [18] Scott M. Lundberg, Gabriel Erion, Hugh Chen, Alex DeGrave, Jordan M. Prutkin, Bala Nair, Ronit Katz, Jonathan Himmelfarb, Nisha Bansal, and Su-In Lee. From local explanations to global understanding with explainable AI for trees. *Nature Machine Intelligence*, 2(1):56–67, 2020.
- [19] Ian Covert and Su-In Lee. Improving KernelSHAP: Practical Shapley value estimation via linear regression. In *International Conference on Artificial Intelligence and Statistics*. PMLR, 2021.
- [20] Fabian Fumagalli, Maximilian Muschalik, Patrick Kolpaczki, Eyke Hüllermeier, and Barbara Hammer. SHAP-IQ: Unified approximation of any-order Shapley interactions. *Advances in Neural Information Processing Systems*, 36, 2024.
- [21] Che-Ping Tsai, Chih-Kuan Yeh, and Pradeep Ravikumar. Faith-Shap: The faithful Shapley interaction index. *Journal of Machine Learning Research*, 24(94):1–42, 2023.
- [22] Mukund Sundararajan, Kedar Dhamdhere, and Ashish Agarwal. The Shapley Taylor interaction index. In *International Conference on Machine Learning*, pages 9259–9268. PMLR, 2020.
- [23] Sebastian Bordt and Ulrike von Luxburg. From Shapley values to generalized additive models and back. In *International Conference on Artificial Intelligence and Statistics*, pages 709–745. PMLR, 2023.
- [24] Hans-Hermann Wessels, Andrew Stirn, Alejandro Méndez-Mancilla, Eric J. Kim, Sydney K. Hart, David A. Knowles, and Neville E. Sanjana. Prediction of on-target and off-target activity of CRISPR–Cas13d guide RNAs using deep learning. *Nature Biotechnology*, 42(4):628–637, 2024.
- [25] Amirali Aghazadeh, Orhan Ocal, and Kannan Ramchandran. CRISPRLand: Interpretable large-scale inference of DNA repair landscape based on a spectral approach. *Bioinformatics*, 36(Supplement_1):i560–i568, 2020.
- [26] Amirali Aghazadeh, Hunter Nisonoff, Orhan Ocal, David H. Brookes, Yijie Huang, O. Ozan Koyluoglu, Jennifer Listgarten, and Kannan Ramchandran. Epistatic Net allows the sparse spectral regularization of deep neural networks for inferring fitness functions. *Nature Communications*, 12(1):5225, 2021.

- [27] David H. Brookes, Amirali Aghazadeh, and Jennifer Listgarten. On the sparsity of fitness functions and implications for learning. *Proceedings of the National Academy of Sciences*, 119(1):e2109649118, 2022.
- [28] Yigit E. Erginbas, Justin S. Kang, Amirali Aghazadeh, and Kannan Ramchandran. Efficiently computing sparse Fourier transforms of q -ary functions. In *2023 IEEE International Symposium on Information Theory (ISIT)*, pages 513–518. IEEE, 2023.
- [29] Andisheh Amrollahi, Amir Zandieh, Michael Kapralov, and Andreas Krause. Efficiently learning Fourier sparse set functions. In *Advances in Neural Information Processing Systems*, volume 32, 2019.
- [30] Michel Grabisch. k -order additive discrete fuzzy measures and their representation. *Fuzzy Sets and Systems*, 92(2):167–189, 1997.
- [31] Gian-Carlo Rota. On the foundations of combinatorial theory: I. theory of Möbius functions. In *Classic Papers in Combinatorics*, pages 332–360. Birkhäuser Boston, 1964.
- [32] Darin Tsui and Amirali Aghazadeh. On recovering higher-order interactions from protein language models. *arXiv preprint arXiv:2405.06645*, 2024.
- [33] Max W. Shen, Mandana Arbab, Jonathan Y. Hsu, Daniel Worstell, Sannie J. Culbertson, Olga Krabbe, Christopher A. Cassa, David R. Liu, David K. Gifford, and Richard I. Sherwood. Predictable and precise template-free CRISPR editing of pathogenic variants. *Nature*, 563(7733):646–651, 2018.
- [34] Xiao Li, Joseph K. Bradley, Sameer Pawar, and Kannan Ramchandran. The SPRIGHT algorithm for robust sparse Hadamard transforms. In *2014 IEEE International Symposium on Information Theory*, pages 1857–1861. IEEE, 2014.
- [35] Tim Künne, Daan C. Swarts, and Stan J.J. Brouns. Planting the seed: target recognition of short guide RNAs. *Trends in Microbiology*, 22(2):74–83, 2014.
- [36] Hans-Hermann Wessels, Alejandro Méndez-Mancilla, Xinyi Guo, Mateusz Legut, Zharko Daniloski, and Neville E. Sanjana. Massively parallel Cas13 screens reveal principles for guide RNA design. *Nature Biotechnology*, 38(6):722–727, 2020.
- [37] Jingyi Wei, Peter Lotfy, Kian Faizi, Sara Baungaard, Emily Gibson, Eleanor Wang, Hannah Slabodkin, Emily Kinnaman, Sita Chandrasekaran, Hugo Kitano, Matthew G. Durrant, Connor V. Duffy, April Pawluk, Patrick D. Hsu, and Silvana Konermann. Deep learning and CRISPR-Cas13d ortholog discovery for optimized RNA targeting. *Cell Systems*, 14(12):1087–1102, 2023.
- [38] Ryan T. Leenay, Amirali Aghazadeh, Joseph Hiatt, David Tse, Theodore L. Roth, Ryan Apathy, Eric Shifrut, Judd F. Hultquist, Nevan Krogan, Zhenqin Wu, Giana Cirolia, Hera Canaj, Manuel D.

- Leonetti, Alexander Marson, Andrew P. May, and James Zou. Large dataset enables prediction of repair after CRISPR–Cas9 editing in primary T cells. *Nature Biotechnology*, 37(9):1034–1037, 2019.
- [39] Eiichiro Sonoda, Helfrid Hohegger, Alihossein Saberi, Yoshihito Taniguchi, and Shunichi Takeda. Differential usage of non-homologous end-joining and homologous recombination in double strand break repair. *DNA Repair*, 5(9-10):1021–1029, 2006.
- [40] Neil Jethani, Mukund Sudarshan, Yindalon Aphinyanaphongs, and Rajesh Ranganath. Have we learned to explain?: How interpretability methods can learn to encode predictions in their interpretations. In *International Conference on Artificial Intelligence and Statistics*, pages 1459–1467. PMLR, 2021.
- [41] Jianbo Chen, Le Song, Martin J. Wainwright, and Michael Jordan. Learning to explain: An information-theoretic perspective on model interpretation. In *International Conference on Machine Learning*, pages 883–892. PMLR, 2018.
- [42] Justin S. Kang, Yigit E. Erginbas, Landon Butler, Ramtin Pedarsani, and Kannan Ramchandran. Learning to understand: Identifying interactions via the Möbius transform. *arXiv preprint arXiv:2402.02631*, 2024.
- [43] Michel Grabisch and Marc Roubens. An axiomatic approach to the concept of interaction among players in cooperative games. *International Journal of Game Theory*, 28:547–565, 1999.

10 Supplementary Materials

Top positive SHAP values			Top negative SHAP values		
Position	Nucleotide	Average SHAP value	Position	Nucleotide	Average SHAP value
5	G	0.120	8	A	-0.079
6	G	0.118	10	A	-0.076
7	G	0.087	6	C	-0.073
25	T	0.080	7	A	-0.071
22	T	0.070	9	A	-0.069
11	C	0.061	20	C	-0.064
21	T	0.061	5	T	-0.055
10	C	0.061	5	C	-0.050
8	G	0.060	6	T	-0.047
3	C	0.058	23	C	-0.045
9	G	0.053	21	C	-0.045
4	C	0.047	3	T	-0.043
8	C	0.043	22	A	-0.042
2	A	0.043	5	A	-0.041
23	T	0.042	25	C	-0.041
4	G	0.037	4	T	-0.041
9	C	0.036	4	A	-0.039
10	G	0.036	18	C	-0.037
24	G	0.032	11	A	-0.037
18	A	0.031	17	C	-0.037

Table S1: Top 20 positive and negative SHAP zero values in TIGER from SHAP zero when predicting the guide score of perfect match target sequences. The top SHAP values are centered around the seed region and are in agreement with KernelSHAP.

Top positive SHAP values			Top negative SHAP values		
Position	Nucleotide	Average SHAP value	Position	Nucleotide	Average SHAP value
6	G	0.123	10	A	-0.066
5	G	0.119	7	A	-0.065
7	G	0.094	8	A	-0.062
11	C	0.076	9	A	-0.062
25	T	0.073	20	C	-0.060
4	C	0.070	6	C	-0.058
10	C	0.062	3	T	-0.046
8	C	0.059	6	T	-0.044
3	C	0.055	9	T	-0.041
8	G	0.054	3	A	-0.040
9	C	0.052	11	A	-0.040
21	T	0.050	5	T	-0.040
22	T	0.049	8	T	-0.038
7	C	0.049	4	A	-0.038
9	G	0.047	22	A	-0.037
4	G	0.046	23	C	-0.037
12	C	0.039	21	C	-0.037
18	A	0.038	10	T	-0.036
10	G	0.037	5	G	-0.036
23	T	0.036	5	C	-0.035

Table S2: Top 20 positive and negative SHAP values in TIGER from KernelSHAP when predicting the guide score of perfect match target sequences. Similar to SHAP zero, the top SHAP values are centered around the seed region.

Top positive interactions			Top negative interactions		
Positions	Nucleotides	Average interaction	Positions	Nucleotides	Average interaction
5,6	G,T	0.061	3,4	C,C	-0.097
5,6	C,A	0.061	8,9	C,C	-0.079
3,4	A,C	0.056	3,4	G,G	-0.061
3,4	C,G	0.055	4,5	G,G	-0.059
19,20	C,A	0.052	4,5	C,C	-0.059
5,6	A,C	0.052	6,7	C,C	-0.059
5,6	T,G	0.052	6,7	G,G	-0.059
19,20	A,C	0.046	5,6	G,G	-0.059
4,5	T,G	0.044	5,6	C,C	-0.059
4,5	A,C	0.044	9,10	T,T	-0.059
8,9	A,C	0.043	19,20	A,A	-0.059
18,19	C,A	0.041	10,11	G,G	-0.057
4,5	G,T	0.038	10,11	C,C	-0.057
4,5	C,A	0.038	9,10	C,C	-0.056
10,11	A,C	0.038	11,12	G,G	-0.056
10,11	T,G	0.038	11,12	C,C	-0.056
8,9	C,G	0.038	8,9	G,G	-0.054
11,12	A,C	0.037	7,8	T,T	-0.052
11,12	T,G	0.037	7,8	G,G	-0.052
6,7	T,G	0.037	7,8	C,C	-0.052

Table S3: Top 20 positive and negative Faith-Shap interactions in TIGER from SHAP zero when predicting the guide score of perfect match target sequences. The top interactions exhibit high GC content around the seed region.

Top positive SHAP values			Top negative SHAP values		
Position	Nucleotide	Average SHAP value	Position	Nucleotide	Average SHAP value
19	T	3.727	19	G	-5.462
19	A	2.466	18	G	-3.105
20	G	2.431	20	C	-2.981
21	A	1.833	21	C	-2.891
22	T	1.754	18	A	-2.617
22	G	1.751	21	A	-2.539
18	T	1.734	17	C	-2.495
21	C	1.733	17	A	-2.495
17	G	1.696	17	T	-2.461
20	A	1.649	22	A	-2.451
18	A	1.527	23	C	-2.266
17	C	1.492	21	G	-2.239
21	G	1.490	22	G	-2.223
18	C	1.490	18	C	-2.138
21	T	1.422	22	T	-2.120
22	C	1.355	22	C	-2.034
23	C	1.220	20	T	-2.001
16	C	1.177	17	G	-1.972
22	A	1.121	20	G	-1.877
17	A	1.104	18	T	-1.775

Table S4: Top 20 positive and negative SHAP values in inDelphi from SHAP zero when predicting the frameshift frequency of DNA target sequences. Top SHAP values are centered around the cut site and are in agreement with KernelSHAP.

Top positive SHAP values			Top negative SHAP values		
Position	Nucleotide	Average SHAP value	Position	Nucleotide	Average SHAP value
19	T	4.383	19	G	-6.148
17	G	4.308	18	G	-4.731
20	G	3.585	23	C	-3.483
18	T	2.773	17	C	-3.212
19	A	2.649	20	C	-2.650
20	A	2.497	21	C	-2.641
22	G	2.359	22	T	-2.534
21	T	2.253	21	A	-2.507
14	G	2.237	17	T	-2.458
21	A	2.161	19	C	-2.305
18	C	2.156	22	A	-2.282
18	A	2.117	20	G	-2.247
21	C	2.085	15	G	-2.235
17	C	2.013	21	G	-2.216
22	T	1.999	20	T	-2.164
23	C	1.921	18	A	-2.144
21	G	1.838	18	C	-2.116
15	T	1.648	26	G	-2.091
14	T	1.580	15	T	-2.009
23	G	1.528	22	G	-1.959

Table S5: Top 20 positive and negative SHAP values in inDelphi from KernelSHAP when predicting the frameshift frequency of DNA target sequences. Like SHAP zero, the top SHAP values are centered around the cut site.

Top positive interactions			Top negative interactions		
Positions	Nucleotides	Average Interaction	Positions	Nucleotides	Average Interaction
18,19,21,22	G,C,G,G	2.504	18,19,21,22	T,C,T,C	-5.640
18,19,21,22	C,G,C,C	2.504	18,19,21,22	A,G,A,G	-5.640
18,19,21,22	A,G,A,C	2.504	18,19,21,22	G,C,G,C	-5.640
18,19,21,22	T,C,T,G	2.504	18,19,21,22	C,G,C,G	-5.640
18,21	G,C	2.073	18,19,21,22	G,G,G,G	-5.640
18,21	C,G	2.073	18,21	G,G	-5.325
17,18,21,22	G,C,G,C	1.983	18,21	C,C	-5.325
17,18,21,22	G,G,G,G	1.983	17,18,20,21	G,A,G,A	-4.658
17,18,21,22	A,A,A,A	1.983	17,18,20,21	T,G,T,G	-4.658
17,18,21,22	A,G,A,G	1.983	17,18,20,21	A,T,A,T	-4.658
17,18,21,22	A,C,A,C	1.983	17,18,20,21	C,A,C,A	-4.658
17,18,21,22	T,T,T,T	1.983	17,18,20,21	T,C,T,C	-4.658
17,18,21,22	T,A,T,A	1.983	17,18,20,21	G,G,G,G	-4.658
18,19,20,21	C,T,C,T	1.982	17,18,20,21	C,G,C,G	-4.658
18,19,20,21	A,G,A,G	1.982	17,18,20,21	G,C,G,C	-4.658
18,19,20,21	C,A,C,A	1.982	17,18,20,21	A,G,A,G	-4.658
18,19,20,21	G,G,G,G	1.982	17,18,20,21	A,A,A,A	-4.658
18,19,20,21	G,A,G,A	1.982	17,18,20,21	T,T,T,T	-4.658
18,19,20,21	T,G,T,G	1.982	17,18,20,21	T,A,T,A	-4.658
18,19,20,21	A,C,A,C	1.982	18,21	T,T	-4.553

Table S6: Top 20 positive and negative Faith-Shap interactions in inDelphi from SHAP zero when predicting the frameshift frequency of DNA target sequences. GCGC and TCTC interactions at positions 17-18 and 21-22 and at 18-19 and 21-22, respectively, show high-order microhomology patterns.

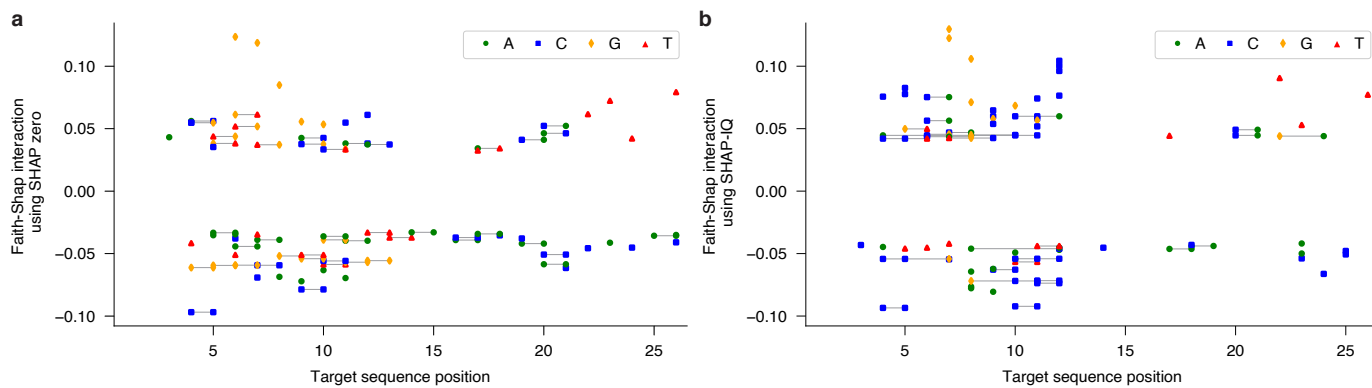


Figure S1: **Top interactions in TIGER.** a, Top 80 Faith-Shap interactions in TIGER with SHAP zero and b, SHAP-IQ. Although overlapping interactions in SHAP zero and SHAP-IQ are in agreement, SHAP zero interactions are more concentrated around the seed region. Source data are provided as Source Data file.

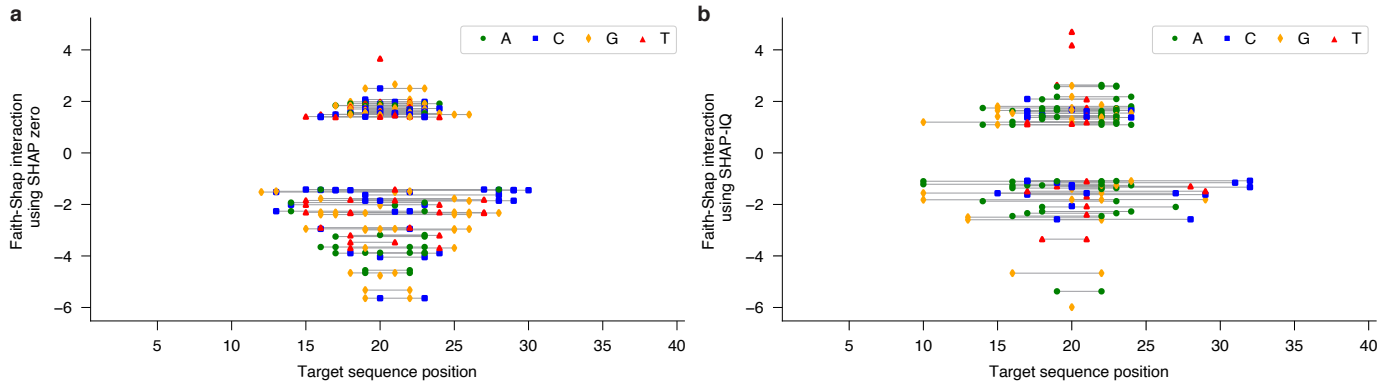


Figure S2: **Top interactions in inDelphi.** **a**, Top 80 Faith-Shap interactions in inDelphi with SHAP zero and **b**, SHAP-IQ. While overlapping interactions are in agreement, the majority of SHAP-IQ interactions are not centered around the cut site. Source data are provided as Source Data file.

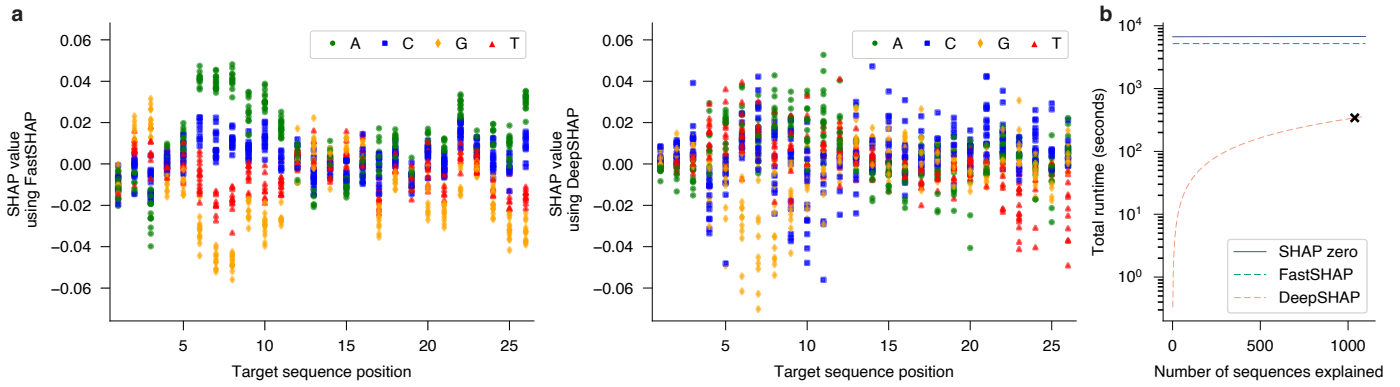


Figure S3: **FastSHAP** and **DeepSHAP** on **TIGER**. **a**, FastSHAP and DeepSHAP estimates over 1038 query sequences, with a random subset of 50 estimates shown for clarity. **b**, Total runtime of SHAP zero, FastSHAP, and DeepSHAP over 1038 target sequences. While both methods are faster than SHAP zero, FastSHAP estimates do not correlate well with KernelSHAP, and DeepSHAP estimates are not black-box and do not support amortized inference. Source data are provided as Source Data file.

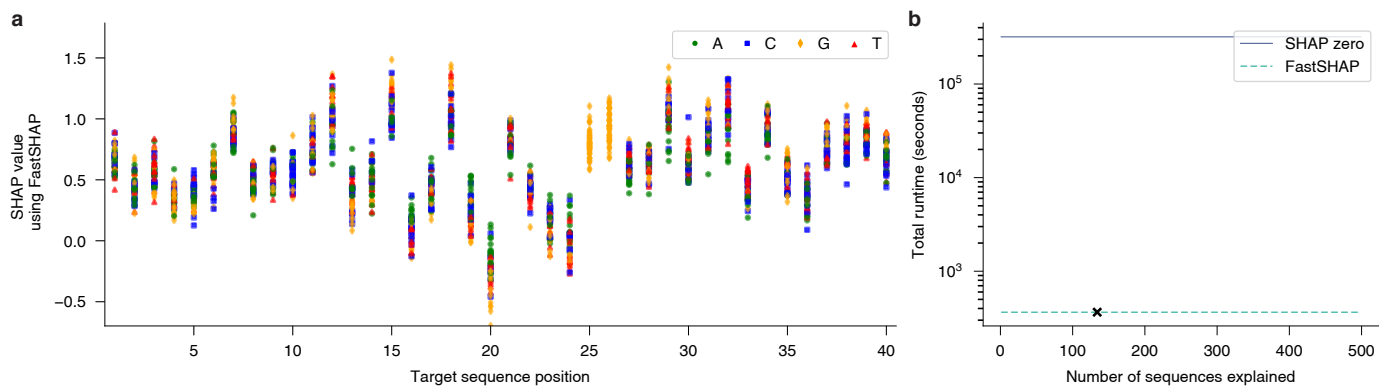


Figure S4: **FastSHAP on inDelphi.** **a**, SHAP values of 40 random target sequences from FastSHAP. **b**, Total runtime of SHAP zero and FastSHAP over 134 target sequences. While FastSHAP is faster than SHAP zero, FastSHAP estimates do not correlate well with KernelSHAP. Source data are provided as Source Data file.